Silicon isotopes in an EMIC's ocean: sensitivity to runoff, iron supply and climate

[1]Institute of Geosciences, Christian-Albrechts-University of Kiel, Ludewig-Meyn-Strasse 10, 24118, Kiel, Germany
[2]GEOMAR Helmholtz Centre for Ocean Research, Kiel, Düsternbrooker Weg 20, 24105, Germany
[3]Potsdam Institute for Climate Impact Research (PIK), Telegraphenberg A62 / 0.04, 14412 Potsdam, Germany
[4]Institute of Marine Research, 1870 Nordnes, NO-5817, Bergen, Norway
[5]Bjerknes Centre for Climate Research, Bergen, Norway

H. Dietze[1,2], U. Löptien[1,2], R. Hordoir[4,5], M. Heinemann[1], W. Huiskamp[3], B. Schneider[1]

Key Points:

- We simulate the isotopic composition of biogenic silica archived in the ocean's sediment.
- Our simulations with an Earth System Model compare modern climate to glacial conditions.
- Out of several hypotheses tested, altering the isotopic composition of runoff during the LGM is most consistent with proxies.

Corresponding author: Heiner Dietze, heiner.dietze@ifg.uni-kiel.de

This article has been accepted for publication and undergone full peer review but has not been through the copyediting, typesetting, pagination and proofreading process which may lead to differences between this version and the Version of Record. Please cite this article as doi: 10.1029/2020PA003960

©2020 American Geophysical Union. All rights reserved.

Abstract

The isotopic composition of Si in biogenic silica (BSi), such as opal buried in the oceans' sediments, has changed over time. Paleo records suggest that the isotopic composition, described in terms of δ^{30}Si, was generally much lower during glacial times than today. There is consensus that this variability is attributable to differing environmental conditions at the respective time of BSi production and sedimentation. The detailed links between environmental conditions and the isotopic composition of BSi in the sediments remain, however, poorly constrained. In this study, we explore the effects of a suite of offset boundary conditions during the LGM on the isotopic composition of BSi archived in sediments in an Earth System Model of intermediate complexity. Our model results suggest that a change in the isotopic composition of Si supply to the glacial ocean is sufficient to explain the observed overall low(er) glacial δ^{30}Si in BSi. All other processes explored triggered model responses of either wrong sign or magnitude, or are inconsistent with a recent estimate of bottom water oxygenation in the Atlantic Sector of the Southern Ocean. Caveats, mainly associated with generic uncertainties in today's pelagic biogeochemical modules, remain.

1 Introduction

Numerical, model-based projections into our warming future suggest ensuing global-scale redistribution of nutrients from the sun-lit surface ocean to depth. Among the prospective consequences are declining biological productivity and fish yields. Disconcertingly, these effects may prevail for a millennium (Moore et al., 2018). But how reliable are such climate projections?

The problem is that we will not live to calculate substantiated statistics on the reliability of climate forecasts. Hence, an approach similar to the one pursued in weather-forecasting, where progress has been accomplished during decades of daily forecasts and subsequent ground-truthing (c.f. Bauer et al., 2015), is not viable – if pressing societal questions are to be answered in time. A straight-forward and generic way to deal with this problem is to assume that fidelity of now-casts is correlated with the fidelity of climate forecasts. This assumption, however, has been challenged, e.g., by Knutti et al. (2009) and Notz (2015) for coupled ocean-atmosphere models and, recently, by Löptien and Dietze (2017) and Löptien and Dietze (2019) for models of pelagic biogeochemical cycling.

A potential solution to this dilemma is the assessment of past climate states to test the sensitivity of climate models (as suggested by, e.g., Braconnot et al., 2012). The idea being that the geologic records of environmental responses to past climate changes complement the climate observations from the past decades such that respective fidelity metrics become indicative of the reliability of future projections.

In this regard, the isotopic composition (δ^{30}Si) of biogenic silica (BSi) preserved in ocean sediments is of special interest to the field of pelagic biogeochemical ocean modeling. The reasons are: first, silicic acid (DSi) is an essential element for diatoms, which are autotrophic key players in the pelagic carbon cycle. Second, the isotopic composition of BSi is stable and preserves over millennia once secluded from processes at the water-sediment interface. Third, diatoms produce BSi with a δ^{30}Si distinctly different from the δ^{30}Si of their substrate DSi. The latter is caused by diatoms which tend to build more isotopically light BSi into their shells, compared to the δ^{30}Si in ambient DSi - a process also referred to as fractionation. This fractionation relates the δ^{30}Si of BSi in the sediments to the turnover of DSi by diatoms. The advantage of using the isotopic composition to improve our current understanding of glacial-interglacial cycles, instead of simply using BSi sediment burial rates, is that δ^{30}Si is less affected by water-column processes which are, on the one hand, unrelated to BSi production but may, on the other hand, modulate the amount of BSi that is preserved in the sediments.

©2020 American Geophysical Union. All rights reserved.

A major challenge is the interpretation of δ^{30}Si of BSi records because the link between diatom DSi turnover and δ^{30}Si isotopic signature in BSi is complex (see also Ragueneau et al., 2000). In a (Rayleigh) system, like a surface mixed layer in spring, diatoms preferentially take up lighter DSi until only relatively heavy substrate is left (and subsequently taken up). Hence, the δ^{30}Si isotopic signature in BSi is indicative of the amount of substrate left, with high (low) values indicating oligotrophic (nutrient replete) conditions. In contrast, in a system characterized by high incoming and outgoing physical transports of substrate (e.g. a location within the Gulf Stream) the δ^{30}Si of BSi is predominantly determined by the δ^{30}Si of the constantly resupplied DSi - and only modestly altered by the respective fractionation during BSi production because the fractionation signal can not build up (since it is constantly flushed out of the local system). Both the Rayleigh and the "flushed" system can be described to high precision by simple equations (e.g. Closset et al., 2016, their equation 1 to 6). The difficulty is in the quantification of the relation between physical transport flushing rate and biotic BSi export out of the sun-lit surface ocean - or in other words: the relation between flushing and BSi production needs to be known in order to interpret δ^{30}Si of BSi records. Further complexity is potentially added by variations of the δ^{30}Si composition of DSi feeding the surface waters.

In summary, both local (production and export of BSi, which is affected by local environmental conditions) and remote processes (production and export upstream which affects incoming environmental conditions), determine the isotopic signature of BSi at a given location. This complex entanglement of ocean circulation and biogeochemistry calls for the application of a 3-dimensional numerical model to guide the interpretation of δ^{30}Si in observed BSi records. Indeed, the (modern climate) pioneering studies of Wischmeyer et al. (2003) and Gao et al. (2016) illustrated the benefit of using a numerical coupled ocean-circulation biogeochemical model in linking silicon isotopes to silicic acid utilization.

Using models for interpretation in such ways leads, however, to a causality dilemma. Coupled ocean-circulation biogeochemical models rely on a number of assumptions and (often poorly known) model parameters (such as growth/death of phytoplankton and sinking of organic matter to depth). Most of these assumptions and parameters are not well constrained in the sense that different choices may result in an equally-good fit to present day observations - but simultaneously very different projections (e.g. Löptien and Dietze (2017), Löptien and Dietze (2019)). Thus, paleo records such as the isotopic composition of BSi preserved in ocean sediments, are of great interest to assess and reduce such uncertainties. At the same time, these model uncertainties complicate the interpretation of simulated past marine biogeochemical cycling in general (e.g., Hülse et al., 2017) and of the isotopic composition of BSi preserved in ocean sediments in particular. An aggravating circumstance is that the observational records are still so sparse (even for present day δ^{30}Si DSi), such that Hendry and Brzezinski (2014) conclude that the data set is "... inadequate to evaluate mechanisms leading to even the first-order distribution of isotopes of Si in the global ocean".

Even so, a number of very interesting hypotheses, explaining aspects of spatial and temporal variance in δ^{30}Si of BSi records, have been rooted on the available observational records. Among them is the Silicic Acid Leakage Hypothesis which may explain glacial interglacial atmospheric CO_2 changes (SALH, e.g., Brzezinski et al. (2002), Matsumoto et al. (2002), Matsumoto et al. (2014)). In the following we outline the basic idea of the SALH as far as the silicic acid is concerned (see, e.g. Matsumoto and Sarmiento, 2008, as concerns it's link to glacial interglacial atmospheric CO_2 changes): Today's Southern Ocean (SO) retains or traps DSi at the expense of more northward latitudes by a combination of deep and efficient BSi export and meridional overturning. Driven by the strong southern westerly wind belt, deep, nutrient replete waters are brought to the surface at the Antarctic Divergence. The northward branch of the Divergence (which po-

©2020 American Geophysical Union. All rights reserved.

tentially exports DSi from the SO) is efficiently stripped of DSi by phytoplankton. So, by the time the water reaches the Polar Front and the formation sites of Subantarctic Mode Waters (SAMW) and Antarctic Intermediate Waters (AAIW) which spread northwards, most of the DSi has been exported as BSi to depth into the southward-flowing Circumpolar Deep Water (CDW). The CDW surfaces south of the Polar Front and, hence, the respective DSi is thereby retained in the SO. The SALH postulates that this DSi trapping in the SO was alleviated during glacial times triggered by e.g. enhanced iron supply: the enhanced iron supply and associated physiological changes may have reduced the Si demands of diatoms, relative to the need of bioavailable nitrogen. Thus, left-over DSi might have leaked into the SAMW and AAIW and thereby could have left the SO. In summary, the SALH assumes that more DSi might have been available outside the SO during glacial times. A straightforward (Rayleigh) conclusion is that the glacial δ^{30}Si was lower (as observed) because, according to the above considerations, DSi should have been less limiting relative to nitrogen.

The SALH and its relation to relatively low glacial δ^{30}Si (e.g., Sutton et al., 2018) has, however, been recently challenged by Frings et al. (2016) who concluded, based on a very comprehensive review, that consistent shifts among different ocean basins from low glacial δ^{30}Si to higher interglacial δ^{30}Si ($0.5 - 1$‰) may rather have been caused by a respective change in the isotopic composition of land-ocean fluxes of Si.

Our study adds to the ongoing discussion by exploring various hypotheses potentially triggering lower glacial δ^{30}Si in an Earth System Model of intermediate complexity. Our modeling approach builds on the pioneering works of Wischmeyer et al. (2003) and Gao et al. (2016) for modern climate and applies our extended model to both the Last Glacial Maximum and modern climate. Specifically, we explore the effects of (1) differences in the Si:N ratios, mimicking alleviated iron limitation during the LGM (Matsumoto et al., 2014), (2) differing winds during the LGM (e.g., Kohlfeld et al., 2012; McGee et al., 2010; Sime et al., 2013), (3) differing Si supply to the ocean during the LGM (Frings et al., 2016) and (4) a differing isotopic composition of Si supplied to the ocean during the LGM (Frings et al., 2016; Opfergelt et al., 2013). The underlying aim is to illustrate the complex entanglement of ocean circulation and biogeochemistry, which finally determines the isotopic composition of δ^{30}Si of BSi preserved in sediments.

2 Materials and Methods

2.1 Observations

We use the World Ocean Atlas 2009 data to assess our preindustrial (*PI*) simulation. More specifically, we compare against annual mean climatologies of temperature (Locarnini et al., 2010), salinity (Antonov et al., 2010), phosphate (Garcia et al., 2010) and silicate (Garcia et al., 2010).

Silicon isotopic data in seawater (δ^{30}Si of DSi) are put together from data published in Beucher et al. (2008,1); Cardinal et al. (2005); De La Rocha et al. (2011); de Souza et al. (2012a,1); Ehlert et al. (2012); Fripiat et al. (2011a,1,1); Grasse et al. (2013); Reynolds et al. (2006). A binning procedure increased horizontal data coverage: surface data with a nominal depth of 50 m refers to binning all data within 0-100 m. Abyssal data refers to binning all data within 1500-2500 m.

Silicon isotopic data in BSi as preserved in sediment cores is compiled, following Frings et al. (2016), from Brzezinski et al. (2002); De LaRocha et al. (1997); De La Rocha et al. (1998, 2011); Ehlert et al. (2013); Ellwood et al. (2010); Hendry et al. (2016,1); Horn et al. (2011); Pichevin et al. (2009).

©2020 American Geophysical Union. All rights reserved.

2.2 Model

In this study we present numerical simulations with the University of Victoria Earth System Climate Model (UVic ESCM, Weaver et al., 2001). We present equilibrium simulations for two distinct climates, the preindustrial year 1800 (PI) and the Last Glacial Maximum (LGM) 21000 years before present and evaluate the model's distribution of δ^{30}Si of BSi preserved in ocean sediments. UVic ESCM is an intermediate complexity model, featuring a simplified (vertically integrated) atmosphere. In contrast, the ocean dynamics is, although rather coarse, resolved in all three dimensions. The vertical resolution starts with 50 m at the surface of the ocean and gradually coarsens to 500 m in the abyss. The horizontal resolution of all model components (i.e., ocean, land, atmosphere, sea ice) is 1.8° in meridional and 3.6° in zonal direction. UVic's assets are low computational demands and an extensive number of peer-reviewed studies including the description of LGM and PI equilibrium simulations. Among its drawbacks are a simplified atmosphere and a spatial resolution of the ocean that is coarse compared to, e.g., that class of models that underlie the current projections of the Intergovernmental Panel on Climate Change. Our simulations build on two configurations introduced by Brennan et al. (2012) already:

(1) *PI*, which refers to the "Preindustrial Equilibrium Simulation" described in Sec. 3 of Brennan et al. (2012). Briefly summarized, the atmospheric $p\mathrm{CO}_2$ is set to 283.87 ppm and the orbital configurations to those representative of the year 1800. The initial conditions are those from the 5 kyr spinup from Brennan et al. (2012).

(2) *LGM*, which refers to the "Last Glacial Maximum Equilibrium Simulation" described in Sec. 4 of Brennan et al. (2012). Briefly summarized, the atmospheric $p\mathrm{CO}_2$ is set to a low 189.65 ppm, the orbital parameters to those representing the conditions at 21 kyr BP and the surface elevation and albedo on land are adjusted following a reconstruction of Northern Hemisphere land ice (ICE-4G, Peltier (2009)).

The wind forcing during LGM consists of the same prescribed climatology (NCEP) used for the preindustrial simulations in our rather simple ESCM (see Weaver et al., 2001, for details). Rather weak dynamic wind feedbacks are parameterized as a function of surface temperature gradients and added to this climatology. The choice of building on a present day climatology is pragmatic, since the wind conditions during the LGM are discussed controversially (e.g. Kohlfeld et al., 2012; Sime et al., 2013).

2.2.1 Equations for the Si-Cycle

For this study we added an explicit and prognostic representation of (1) dissolved silicic acid (DSi), (2) biogenic Si (BSi), (3) that fraction of DSi that is composed of the silicon isotope ^{30}Si ($\mathrm{D}^{30}\mathrm{Si}$) and (4) that fraction of BSi that is composed of the silicon isotope ^{30}Si ($\mathrm{B}^{30}\mathrm{Si}$) to the original pelagic biogeochemical module used in Brennan et al. (2012). All prognostic biogeochemical variables C, at a given point in (model) space are determined following:

$$\frac{\partial C}{\partial t} = T + sms, \tag{1}$$

where T denotes the spatial divergence of diffusive and advective transports. *sms* refers to the source-minus-sinks term. The *sms* terms of the silicon module are adopted from Gao et al. (2016). The convenience of their approach is that the silicon module does not feed back onto the original biogeochemical model (of, in our case, Brennan et al. (2012)). Thus, our silicon isotope module is purely diagnostic in the sense that it does not alter the original climate and carbon cycles documented by Brennan et al. (2012) already.

The respective *sms* terms that describe the linkage of the silicic acid cycle with the pelagic biogeochemical cycle of Brennan et al. (2012) are described below. Approach and notation follow Gao et al. (2016). The DSi is supplied to the ocean at a temporally con-

©2020 American Geophysical Union. All rights reserved.

Accepted Article

stant rate, $RRDSi$ of $9.55\,Tmol\,Si\,year^{-1}$ (Frings et al., 2016) and is homogeneously distributed over the surface ocean.

- **DSi equation:**

$$sms(DSi) = r\,BSi - P_{Si}, \tag{2}$$

where r denotes the diatom opal dissolution rate and P_{Si} denotes the biogenic opal production. r is temperature dependent:

$$r = A\,\exp\left(T/T_c\right), \tag{3}$$

with the parameters A setting the dissolution rate and T_c determining the temperature dependance of opal dissolution. The value of T_c is adopted from Gao et al. (2016) (see Table 1). The value of A has been determined in a tuning exercise (see Section 2.2.2), P_{Si} is calculated as a function of the production rate of particulate organic matter *pomp* (as calculated by the original biogeochemical module of Brennan et al., 2012) and DSi concentration:

$$P_{Si} = \min\left(pomp\,R_{Si:P}\frac{DSi}{K_{PHY}^{DSi} + DSi}, r_{Pro}\,DSi\right), \tag{4}$$

where, $R_{Si:P}$ denotes the molecular DSi to phosphate uptake ratio, associated with BSi production, K_{PHY}^{DSi} denotes the half-saturation constant of DSi uptake (see Table 1). r_{Pro} is the maximum rate of BSi production under non-limiting conditions.

- **BSi equation**:

$$sms(BSi) = -r\,BSi + P_{Si} - w\frac{\partial BSi}{\partial z}, \tag{5}$$

where, w is the sinking speed of BSi and $w\frac{\partial BSi}{\partial z}$ denotes the divergence of vertical BSi fluxes.

- **D^{30}Si equation:**

Following Gao et al. (2016) we include, in addition to total Si (i.e. the sum of the stable isotopes ^{28}Si, ^{29}Si, and ^{30}Si), an explicit representation of the silicon isotope ^{30}Si. During BSi production we apply the fractionation factor $\alpha_1 = 0.9989$ (De LaRocha et al., 1997; Gao et al., 2016) which reduces the uptake of heavier ^{30}Si relative to the lighter Si stable isotopes.

$$sms(D^{30}Si) = r\,BSi\frac{B^{30}Si}{BSi} - P_{Si}\,\alpha_1\frac{D^{30}Si}{DSi} \tag{6}$$

Following Gao et al. (2016), we assume no fractionation during BSi dissolution.

- **B^{30}Si equation:**

$$sms(B^{30}Si) = -r\,BSi\frac{B^{30}Si}{BSi} + P_{Si}\,\alpha_1\frac{D^{30}Si}{DSi} - w\frac{\partial B^{30}Si}{\partial z}. \tag{7}$$

We calculate the silicon isotopic composition $\delta^{30}Si$ in units ‰ as a function of the total DSi (or BSi) concentration and D^{30}Si (or B^{30}Si) following:

$$\delta^{30}Si = \left(\frac{(^{30}Si/^{28}Si)_{sample}}{(^{30}Si/^{28}Si)_{NBS-28}} - 1\right)\cdot 10^3, \tag{8}$$

©2020 American Geophysical Union. All rights reserved.

$(^{30}Si/^{28}Si)_{NBS-28} = 0.0335$ (Coplen et al., 2002). We calculate ^{28}Si from the total Si and ^{30}Si concentrations as $^{28}Si = 0.953(Si - ^{30}Si)$ which assumes that all stable isotopes other than the ^{28}Si and ^{30}Si always amount to 4.7% of total Si. (Here we follow Reynolds, 2009, stating that the assumption of a constant relative abundance of the normalizing isotope "... is valid for small isotopic variations described by the δ notation".)
We set the isotopic composition $\delta^{30}Si$ of DSi supplied to the surface ocean (mimicking e.g. river runoff) RRδ^{30} to 0.74 (Frings et al., 2016).

Our implementation of processes in the sediments is idealized. Once BSi sinks out of the lowermost wet model grid box it gets buried and leaves the system forever. A constant surface flux RRDSi (Table 1) replenishes what is lost by sedimentation - if the integration is long enough so that the model can reach an equilibrium. Simulated $\delta^{30}Si$ of sedimented BSi are taken as the simulated isotopic composition of BSi sinking out of the lowermost wet model grid box. This idealization is motivated by the urge to save computational resources that would otherwise be necessitated to equilibrate the sediment model.

2.2.2 Parameter Settings

The volume of the ocean is $1.4{\cdot}10^{18}\,m^3$, containing an average DSi concentration of $92\,mmol\,Si\,m^{-3}$ (Garcia et al., 2010). This yields an oceanic inventory of $1.3{\cdot}10^{17}\,mol\,Si$. Devision of the inventory with the supply rate of DSi (RRDSi, Table 1) to the ocean yields a timescale of 14 000 years. This timescale is a rough estimate of the residence time of DSi in the ocean consistent with the 9 000 to 16 000 year range estimated by Georg et al. (2009) and Tréguer et al. (1995), respectively. The residence time of DSi provides a lower bound on the time our model framework needs to adjust to changes to the formulation of Si cycling. It is also a measure of the expected equilibration timescale of the model.

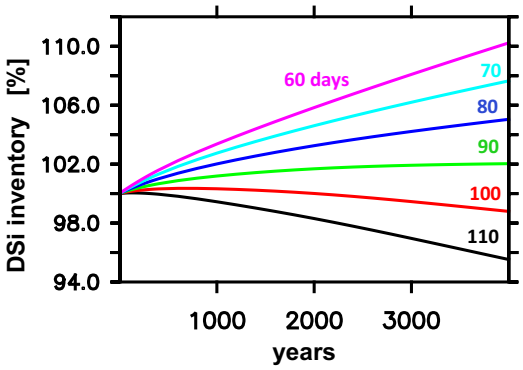

Figure 1. Temporal evolution of simulated preindustrial oceanic DSi inventory relative to observations (WOA09 Garcia et al., 2010, also used to initiate the model) in units %. The different colors denote simulations with different opal dissolution rates (i.e. different choices of parameter A in Table 1). The colored numbers denote the respective inverse of parameter A in units days.

The long equilibration timescale of our Si module calls for long wall-clock times until the effects of model changes can be evaluated reliably. This limits the number of model parameters (and formulations) that can be explored. Our approach here is to use the original model formulations and parameters from Gao et al. (2016) and to adjust only the opal dissolution rate A, such that the DSi inventory stays close to the observations from

©2020 American Geophysical Union. All rights reserved.

Accepted Article

Table 1. Reference model parameters of our implementation of the Gao et al. (2016) silicon module into the pelagic biogeochemical module of Brennan et al. (2012).

parameter	description	Gao et al. (2016)	our value	unit
A	opal dissolution rate	333^{-1}	90^{-1} (see Fig. 1)	day^{-1}
T_c	critical temperature of opal dissolution	12	12	°C
$R_{Si:P}$	molecular DSi to phosphate stoichiometric ratio	25	25	$\frac{mol\,DSi}{mol\,P}$
K_{PHY}^{DSi}	half-saturation constant of DSi uptake during BSi production	4	4	$\frac{mmol\,DSi}{m^3}$
r_{Pro}	BSi production rate under non-limiting conditions	0.5	0.5	day^{-1}
w	sinking speed of BSi	10	10	$\frac{m}{day}$
RRDSi	total Si supply to the (surface) ocean (by e.g. river runoff)	9	9.55 (Frings et al., 2016)	$\frac{Tmol\,Si}{year}$
RRδ^{30}	isotopic composition of (riverine) Si supply to the (surface) ocean	0.8	0.74 (Frings et al., 2016)	‰
α_1	^{30}Si fractionation factor during BSi production	0.9989	0.9989	[ ]
[ ]	fractionation factor during BSi dissolution	1	1	[ ]

©2020 American Geophysical Union. All rights reserved.

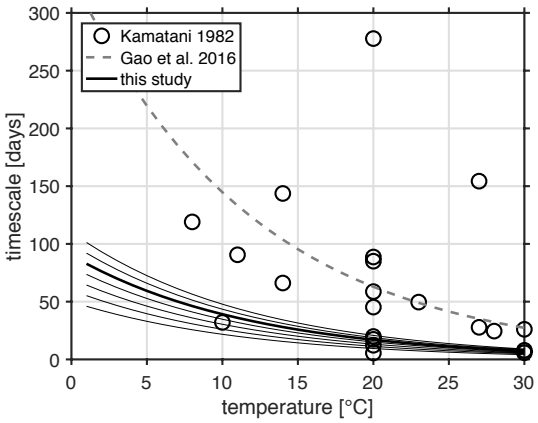

Figure 2. Inverse of dissolution rates of silica from diatoms as a function of ambient temperature. The circles denote data compiled by Kamatani (1982). Three values in excess of 300 days have been discarded here. The dashed grey line refers to settings in the model of Gao et al. (2016). The thick black line refers to the reference model setting in this study. The thin thick lines refer to settings tested during tuning the DSi inventory.

Garcia et al. (2010). Fig. 1 shows that, to this end, the choice of $A = 90^{-1}$ days^{-1} is the best compromise between fast equilibration (which saved wall-clock time) and small misfit to observations (only two % overestimation of DSi inventory) among the choices of A tested in this study.

Fig. 2 shows the temperature dependance of silica dissolution rates that is associated with our choice of A: compared with Gao et al. (2016), our choice features substantially faster dissolution rates, throughout the entire range of temperatures. When compared to data compiled by Kamatani (1982) it is, however, still consistent with observations. On these grounds we justify our choice of $A = 90^{-1}$. We provide a respective model assessment for the Si module in the Appendix A.

2.2.3 Experiments

As outlined above (Sect. 2.2), we run our reference model version under PI and LGM climate conditions to quasi-equilibrium (simulations *PI* and *LGM*). In a second step, starting from *LGM*, we perform a suite of sensitivity experiments for the LGM. Table B.1 lists these experiments, tailored to explore the sensitivity of our model towards environmental changes. The focus is on changes that have been suggested in the literature to have engrained substantial signatures in the isotopic composition of δ^{30}Si of the BSi archived in oceanic sediments. These simulations are setup as follows:

- *LGMfe* is designed to mimic the effect of iron replete conditions on DSi uptake. As summarized by Matsumoto et al. (2014), there is evidence from incubation experiments that the Si:N consumption ratio is high under iron-depleted conditions (Franck et al., 2000; Hutchins and Bruland, 1998) and relatively low under iron replete conditions (Franck et al., 2000; Pondaven et al., 2000). In experiment *LGMfe* the molecular DSi to phosphate stoichiometric ratio $R_{Si:P}$ is reduced by 36%. Because the N:P ratio is fixed to 16 in our model, this corresponds to a Si:N ratio of 1.

- *LGMbreezy* and *LGMslack* are designed to test the effect of potential glacial interglacial variability of climatological winds driving the ocean circulation: The wind

©2020 American Geophysical Union. All rights reserved.

Accepted Article

conditions during the LGM remain poorly constrained, such that even the sign of changes relative to today's conditions is uncertain (e.g. Kohlfeld et al., 2012; McGee et al., 2010; Sime et al., 2013). In order to envelope the range of potential effects on δ^{30}Si of BSi, we follow Matsumoto et al. (2014) and test both a global doubling of wind speeds and a halving, dubbed *LGMbreezy* and *LGMslack*, respectively. These changes affect only the momentum received by the ocean.

- *LGMflush* and *LGMtrickle* are designed to test the effect of potential glacial interglacial variability of riverine Si inputs into the ocean. Following Frings et al. (2016), who suggest, based on a literature review, that the river DSi flux has been within ±20% of today's inputs during the LGM, we increase (decrease) the total supply of Si to the surface ocean by 20% in experiment *LGMflush* (*LGMtrickle*). Because reliable data regarding the variability of the spatial distribution of this input over time is sparse we distribute all input evenly over space.
- *LGMlight* is designed to test the idea of Frings et al. (2016) that the relatively low values of δ^{30}Si archived in glacial BSi are caused by an isotopically lighter composition of riverine Si inputs to the ocean. Following Frings et al. (2016), *LGMlight* reduces the δ^{30}Si of DSi supplied to the ocean by 1‰. The underlying idea is that biotic and abiotic processes acting along the course of a river determine the isotopic composition of the runoff to the ocean. To this end, the study of Schoelynck et al. (2019) is a illustrative curiosity showing the effect of a single herd of hippos increasing δ^{30}Si by a sizable 0.2‰ in Mara River, Kenya. Further, there is evidence that the isotopic composition of groundwater inputs (Georg et al., 2009) and glacial meltwaters (Hawkins et al., 2018) may also have changed over glacial-interglacial cycles (Georg et al., 2009).

2.3 Manifestation Timescales

Our model investigations are all based on numerical time-slice experiments (i.e., we run the model to quasi-equilibrium under the respective boundary conditions) - as opposed to investigating transient responses. Such an approach discards the information regarding the timescales on which model responses to disturbances manifest themselves. This can spuriously illuminate links between processes and their manifestation in the isotopic composition of material archived in sediment cores. We thus measure "manifestation timescales" by locally fitting exponential functions to the simulated δ^{30}Si-anomalies in BSi of the 10 000 year sensitivity experiments, listed in Table 2. Depending on the sign of changes in δ^{30}Si in BSi we fit either to:

$$f(t,x,y) = \alpha(x,y)e^{-\frac{t}{\tau(x,y)}}, \tag{9}$$

or

$$f(t,x,y) = \alpha(x,y)\left(1 - e^{-\frac{t}{\tau(x,y)}}\right), \tag{10}$$

where $f(t,x,y)$ is the accumulated change in δ^{30}Si of BSi at time t, longitude x and latitude y. The constant $\alpha(x,y)$ and the manifestation timescale $\tau(x,y)$ are estimated by using an unconstrained nonlinear minimization of the root mean square deviation between the local exponential fit and simulated local changes in δ^{30}Si in BSi (Nelder–Mead, described in e.g. Lagarias et al., 1998, starting with an initial guess of $\tau = 100\,years$ and $\alpha(x,y)$ as the difference of δ^{30}Si-anomalies between the start and the end of respective time slice experiments).

3 Results

In the following subsections we explore the results of the sensitivity experiments regarding their ability to reproduce observed differences in the δ^{30}Si signature between

©2020 American Geophysical Union. All rights reserved.

Accepted Article

Table 2. Model simulations.

tag	description	initial conditions	duration of simulation
PI	"Preindustrial Equilibrium Simulation" of Brennan et al. (2012)	equilibrated simulation of Brennan et al. (2012)	10000 yr
LGM	"Last Glacial Maximum Equilibrium Simulation" of Brennan et al. (2012)	equilibrated simulation of Brennan et al. (2012)	20000 yr
LGMfe	identical to *LGM* except for Si:N stoichiometric ratio reduced to 1, mimicking the effect of iron replete conditions	end of LGM	10000 yr
LGMbreezy	identical to *LGM* except for a doubling in all winds, driving the oceanic circulation	end of LGM	10000 yr
LGMslack	identical to *LGM* except for a halving of all winds, driving the oceanic circulation	end of LGM	10000 yr
LGMflush	identical to *LGM* except for 20% increase in land-ocean DSi supply	end of LGM	10000 yr
LGMtrickle	identical to *LGM* except for 20% decrease in land-ocean DSi supply	end of LGM	10000 yr
LGMlight	identical to *LGM* except for a 1‰ decrease in δ^{30}Si of land-ocean DSi supply	end of LGM	10000 yr

©2020 American Geophysical Union. All rights reserved.

LGM and PI. Each of the sensitivity experiments builds on a scenario of environmental LGM conditions proposed earlier in the literature (see Section 2.2.3; Table B.1). The major aim is to dissect mechanisms that lead to reasonable agreement with the observations and paleoarchive data.

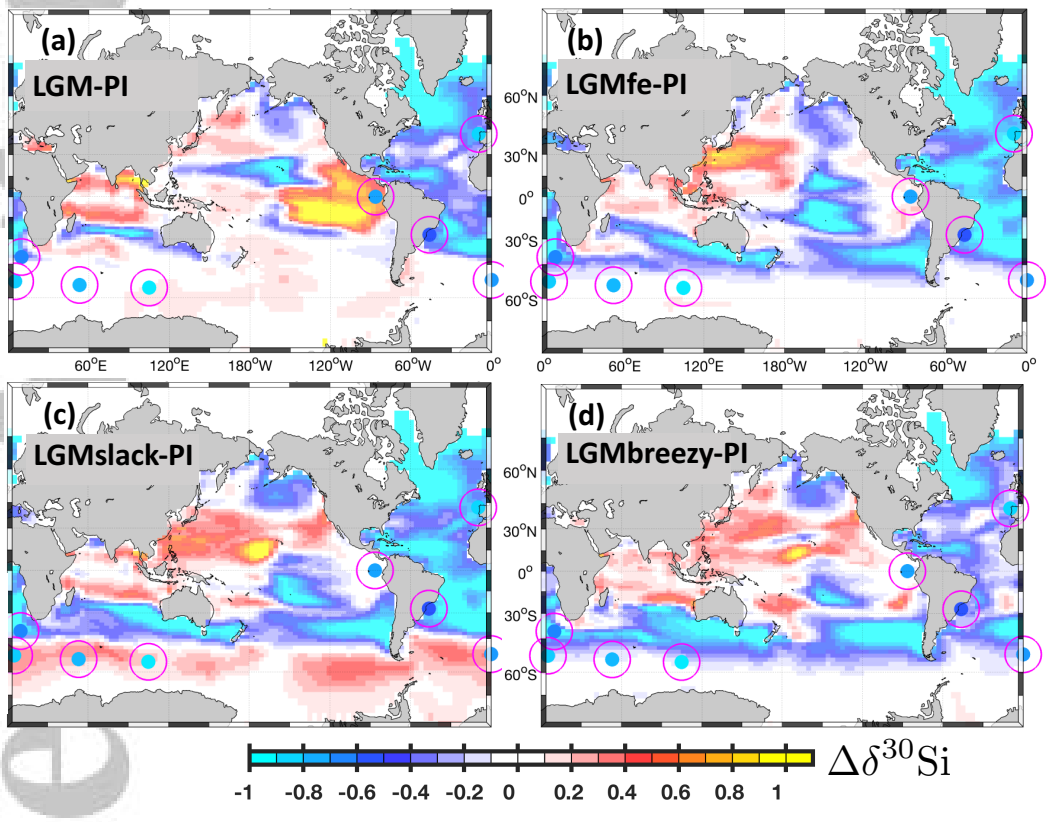

Figure 3. Difference in simulated δ^{30}Si of BSi relative to the preindustrial simulation *PI* as deposited to sediments in units ‰. Panel (a), (b), (c) and (d) refer to differences *LGM-PI*, *LGMfe-PI*, *LGMslack-PI* and *LGMbreezy-PI*, respectively. Magenta circles denote locations of observations of δ^{30}Si in BSi as preserved in sediment cores (see Section 2.1).

3.1 LGM

Figure 3 panel (a) shows the difference between the LGM "reference" simulation *LGM* and our preindustrial simulation *PI*. We find that the colder glacial climate, overall, increases δ^{30}Si of BSi deposited to the sediments (relative to PI). This is inconsistent with observations typically featuring lower glacial δ^{30}Si. (An exception to this rule is the Atlantic Ocean where simulated glacial δ^{30}Si of BSi are lower and roughly consistent with observations.)

In order to set a reference point for the following discussions (in this Section) we dissect the processes that imprint the wrong sensitivity into simulation *LGM*: key to understanding is that *LGM* features an oceanic DSi inventory that is 15% lower relative to that in *PI*. This is puzzling because the export of BSi across 120 m depth (which constitutes the origin of all BSi sinking to depth) is also reduced by a substantial 30% during the colder LGM climate. Given that the riverine supply of Si is identical in *LGM* and *PI*, this is counterintuitive. Further investigations revealed that the process behind this

©2020 American Geophysical Union. All rights reserved.

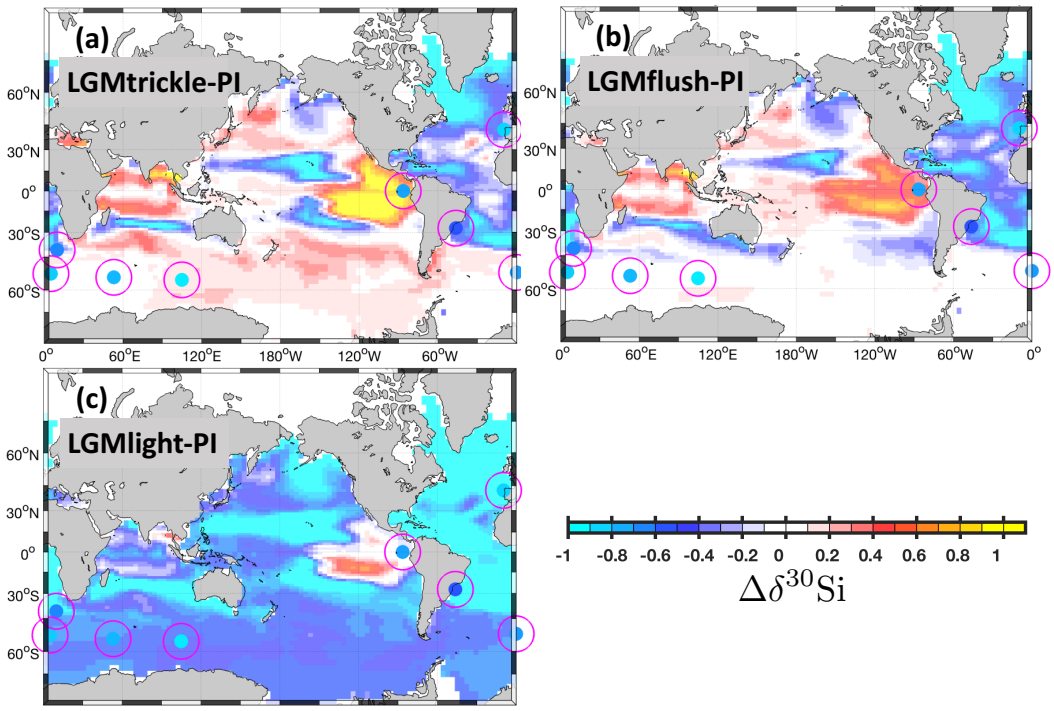

Figure 4. Difference in simulated δ^{30}Si of BSi relative to the preindustrial simulation *PI* as deposited to sediments in units ‰. Panel (a), (b) and (c) refer to differences *LGMtrickle-PI*, *LGMflush-PI* and *LGMlight*, respectively. Magenta circles denote locations of observations of δ^{30}Si in BSi as preserved in sediment cores (see Section 2.1).

conundrum is the antagonistic effect of temperature on BSi sedimentation rate in our model framework. *LGM* features, consistent with observational evidence (e.g., Margo Project Members, 2009), an average of 2°C colder oceanic temperature than *PI*. In combination with an increase in sea-ice cover during the LGM, which shields the ocean from photosynthetically active radiation essential for autotrophic growth, this slows down the global primary production and associated export of organic material from the sun-lit surface to depth. Hence, less BSi is produced and less BSi is set on its way sinking to the sediments. This reduction in BSi production is, however, overcompensated by a remineralization rate that is also slowed down by the lower temperatures such that more organic material reaches the seafloor before it is remineralized and dissolved. A rough scaling, assuming steady state (and horizontal uniformity which reduces the problem to one spatial dimension), puts the potential of this effect into perspective: the vertical flux of sinking BSi described in Equation 5 is, following the notation of Kriest and Oschlies (2008), given by

$$F(z') = F_0 \exp(-\frac{r z'}{\overline{w}}), \tag{11}$$

where $F(z')$ is the sinking flux at depth z' defined as that distance between actual depth and the depth of the euphotic zone. F_0 is the flux out of the euphotic zone. The sinking speed $\overline{w}$ is $10\,m\,day^{-1}$ (see Table 1), and r as defined by our Equation 3. For an ocean with a uniform temperature of 4°C Equation 11 (such as in *PI*) yields a sedimentation efficiency (here defined as the ratio between flux to the sediment and export out of the euphotic zone) of 2‰. A reduction of temperature down to 2°C (such as in *LGM*) yields 5‰. Hence, a reduction of only 2°C yields a substantial (initial) 2.5-fold increase in respective sedimentation rates. It is this temperature-driven increase in sedimentation ef-

©2020 American Geophysical Union. All rights reserved.

ficiency that reduces the global availability of DSi and, consequently, increases overall δ^{30}Si in our *LGM* simulation relative to *PI*.

As concerns the decreasing δ^{30}Si of BSi in the Atlantic Ocean, which outweighs the globally-reversed trend, we find: north of 55° N the simulated DSi inventory is substantially higher during the LGM, relative to PI (Figure A.3). This is owed to fundamentally different global circulation patterns in *PI* and *LGM*. In *PI* the upper branch of the meridional overturning circulation (MOC) supplies the North Atlantic with surface waters that are already relatively depleted in DSi because of biologically induced BSi export from the surface to depth. The lower branch of the MOC exports deep waters enriched in BSi such that the DSi content of the Atlantic Ocean is relatively low. Simulation *LGM* differs in that sea ice protrudes down to 52°N (in winter) which shields respective algae from essential photosynthetically active radiation. This reduced vertical export of BSi meets throttled meridional overturning circulation (2 Sv versus 18 Sv in the simulation *PI*) which puts an end to the cycle that reduces the DSi inventory of the Atlantic Ocean. The supply of DSi to the surface ocean is identical in *PI* and *LGM*. It has a prescribed, relatively (compared to surface values in the North Atlantic) low δ^{30}Si value of 0.74‰ and is evenly distributed over the ocean in our model (see Section 2.2.1). This eventually reduces the δ^{30}Si of BSi in the glacial Atlantic Ocean because it is no longer (or far less) counteracted by the peculiar interplay between biology and MOC described above.

3.2 LGMfe

The simulation *LGMfe* anticipates that more bioavailable iron was available during the LGM. We mimic this effect by reducing the DSi demands by 36% relative to the nitrogen (and phosphorous) demands in our model. This decelerates the biogeochemical cycling of DSi which - according to the Silicic Acid Leakage Hypothesis (SALH) - would reduce the DSi trapping efficiency of the SO. The basic idea behind today's relatively efficient DSi trapping in the SO is that surface waters on their way north out of the SO get depleted of nutrients (DSi) by biologic (BSi) export to depth into southward moving water masses, thereby "trapping" DSi in the SO. By decelerating the cycling of DSi (e.g. by reducing the Si quota in sinking organic matter), the major trapping mechanism is weakened and the hypothesis is that this results in net DSi export, or leakage, out of the SO.

We define a measure of leakage or respective reduction in the "DSi trapping efficiency" as the ratio between oceanic inventory south of 40°S and the total global DSi inventory. Comparing *LGMfe* with *LGM* we find a reduction of only one percent . This rather minute change is outweighed by the effect of the the 36% reduction in DSi demands, described above, which leads to a substantially damped biogeochemical DSi cycling and a reduction of BSi export to the sediments. The latter results in a global increase in the oceanic DSi content of 11%. Hence, even though the trapping efficiency in the SO is reduced, the SO does not lose DSi but rather gains $\approx$ 10% relative to simulation *LGM*. The increase in both local (in the SO) and global DSi concentrations triggers an overall decrease in δ^{30}Si of BSi (Fig. 3 panel (b)) which is generally roughly consistent with observations as far as the sign of changes in concearned. An exception being the SO, where simulated changes are too weak, and at some locations even of opposite sign when compared to the observations.

3.3 LGMslack and LGMbreezy

The simulations *LGMslack* and *LGMbreezy* assume, in contrast to the reference simulation, that glacial winds differed from those today. Sign and magnitude of the change is controversially discussed in the literature. Here we test both, a global halving *LGMslack* and a doubling *LGMbreezy* of wind speeds. The results are depicted in Fig. 3, pan-

©2020 American Geophysical Union. All rights reserved.

els (c) and (d), with *LGMslack* featuring a generally higher δ^{30}Si of BSi in the SO, suggesting a straightforward underlying process: reduced winds bring less DSi up to the sunlit surface which increases the effect of fractionating DSi uptake by algae in surface DSi (because there is less "flushing" of the system). As the substrate (surface DSi) becomes higher in δ^{30}Si, so does the associated BSi export.

In contrast, in *LGMbreezy* more DSi is upwelled in the SO. The effect of fractionation on the isotopic composition of the substrate is diluted by the additional DSi supply. As a consequence δ^{30}Si of BSi mostly decreases and is consistent with observations in terms of the sign of simulated changes. But specifically in the SO *LGMbreezy* features a sensitivity which is apparently too low.

Complexity is added to the rest of the ocean as the system adjusts: enhanced (decreased) upwelling of nutrients by winds feed an increase (decrease) in export production which results in a global Si loss (gain) by increased (decreased) sedimentation such that the initial nutrient pulse is counteracted. Negative values, both in *LGMslack* and *LGMbreezy* follow the overall patterns already discussed for *LGM*.

In summary, our model suggests that reduced winds are inconsistent with observed δ^{30}Si of BSi in the SO. In contrast, the effect of increasing winds appear to be more consistent with the observations of δ^{30}Si of BSi as far as the sign of changes is considered. In terms of magnitude, however, a doubling of the wind during the LGM fails to retrace most of the observations in the SO.

3.4 LGMtrickle and LGMflush

The experiments *LGMtrickle* and *LGMflush* assume that the supply of Si to the glacial ocean was different from today's. The default value (applied in all of our configurations except the two discussed here) for total supply of Si to the ocean (RRDSi) is $9.55\,Tmol\,Si\,year^{-1}$ with an isotopic composition corresponding to 0.74‰ (RRδ^{30}; Table 1). The fractionating effect of marine biota increases the global mean δ^{30}Si of DSi relative to the supply because it preferentially exports BSi with lower δ^{30}Si to the sediment such that DSi with higher δ^{30}Si remains in the water column. From this we conclude that the larger (smaller) the supply in relation to the biotic turnover the lower (higher) the δ^{30}Si in DSi - which ultimately controls the isotopic composition of BSi archived in sediments.

Fig. 4 supports this conclusion: panel (a) shows the difference between the simulation *LGMtrickle* and *PI*. Compared to panel (a) in Fig. 3, we find that the 20% reduction of Si supply to the ocean drives an overall increase in δ^{30}Si of BSi. Likewise, panel (b) in Fig. 4 shows that a 20% increase in Si supply decreases the overall δ^{30}Si of BSi with the biggest effect concentrated in the eastern equatorial upwelling area.

In summary, the sensitivity of δ^{30}Si of BSi to changes in Si supply is too small to explain observed glacial interglacial variations. Expressed in terms of a global average of δ^{30}Si of BSi, we find less than 0.1‰ change when altering the Si supply by 40% in Si.

3.5 LGMlight

Frings et al. (2016) suggest that the relatively low δ^{30}Si of BSi archived in glacial sediments are caused by a glacial isotopic composition of the Si supplied to the ocean that was 1‰ lighter than today. Consistent with their reasoning, we find in Fig. 4 panel (c) a global decrease in δ^{30}Si of BSi by up to 1‰ (with the eastern tropical Pacific being an exception) in response to the reduction of RRδ^{30}. Expressed in terms of a global oceanic average we find a decrease of 0.65‰ at the end of our 10 000 year spinup.

©2020 American Geophysical Union. All rights reserved.

In summary, Fig. 4 panel (c) suggests that a reduction of δ^{30}Si in DSi supplied to the ocean drives changes that are consistent with almost all observations of glacial δ^{30}Si in BSi archived in sediments.

4 Discussion

In Section 4.1 we discuss timescales at work, Section 4.2 puts the results into perspective and Section 4.3 discusses potential and generic sources of uncertainties in the underlying Earth System Model.

4.1 Manifestation Timescales

So far we explored the sensitivity of our model to changes in environmental conditions with numerical time-slice experiments. This can be deceptive for, e.g., processes that manifest themselves with timescales as long or longer than typical glacial interglacial cycles. In the following we use the concept of manifestation timescale introduced in Section 2.3. in order to check if our simulated isotopic signatures of processes could possibly be detected in actual sediments - as opposed to being smeared out over one or more glacial interglacial cycles.

Fig. 5 shows that manifestation timescales vary considerably over space. In terms of detectability, we find in *LGMlight* that manifestation timescales at the observational sites are short enough so that they should be detectable in sediments (if they were to have been at play). This suggests that the effect of changing isotopic composition of oceanic Si supply to the ocean would be clearly imprinted into the sediment record. This does not apply to *LGMbreezy* where manifestation timescales in the Southern Ocean exceed

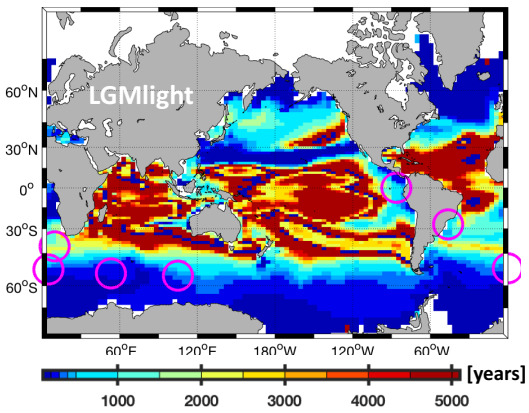

Figure 5. Timescale of manifestation of changes in δ^{30}Si of BSi archived in sediments simulated in *LGMlight* (as shown in Figure 3 panel c) in units years. White patches denote changes of less than 0.1‰ or regions with bottom BSi concentrations less than $10^{-10}\,mol\,Si\,m^3$. Magenta circles denote locations of observations of δ^{30}Si in BSi as preserved in sediment cores (see Section 2.1).

4.2 Appraisal of Results

The two experiments *LGMbreezy* and *LGMlight*, out of our total of 7 numerical sensitivity experiments, feature the best fit with respect to the sign to the overall, lower (rel-

©2020 American Geophysical Union. All rights reserved.

ative to today) glacial δ^{30}Si of BSi observations. This holds especially in the Southern Ocean. The experiment with increased winds (*LGMbreezy*), however, features a sensitivity which, although of correct sign, is much lower than suggested by observational evidence. In addition *LGMbreezy* features very long manifestation timescales (when compared to *LGMlight*; cf., Sect. 4.1) which implies that the process of increasing winds is, in reality, even harder to detect than the rather weak signal we find at the end of our 10 000 year long numerical time slice experiment suggests. This leaves us with simulation *LGMlight* being the most consistent with observations of δ^{30}Si of BSi out of all considered processes (listed, e.g., in Table B.1).

Even so, other processes such as changes to air-sea iron fluxes and wind fields may also have been at play. According to our model results, however, these should manifest themselves more prominently in metrics other than in the isotopic composition of BSi. One example of such a metric are sedimentary redox-sensitive trace-metal records. Jaccard et al. (2016) deduce from respective evidence glacially reduced dissolved oxygen concentrations in the Atlantic Sector of the deep SO. Figure 6 suggests that, in our model, a decrease in wind speeds does drive a consistent oxygen decrease while unchanged winds, or an increase of winds, result in an inconsistent increase of simulated dissolved oxygen concentrations. Investigations of the link between decreasing winds and oxygen reveals two antagonistic processes being at work in our model. For one, the reduced wind-induced upwelling of nutrients drives less production and associated oxygen consumption in the SO. This, on its own, would increase the oxygen concentration. However, this process is opposed by a reduced wind-induced overturning which reduces ventilation and drives an oxygen decrease. The net effect differs among the sectors of the SO, such that the Atlantic Sector in Figure 6 panel (b) is consistent with results from Jaccard et al. (2016). The difference among the Sectors in the SO is facilitated by a reduced (down to 40% relative to *LGM*) Antarctic Circumpolar Current which reduces the zonal mixing between the Sectors as a result of reduced winds supplying less momentum to the ocean. Please note that a comprehensive analysis of oceanic deoxygenation, which must cover the role of (preferably explicitly resolved) iron dynamics (see, e.g. Stoll, 2020) and more data (e.g. Jaccard and Galbraith, 2011), is beyond the scope of this manuscript which focuses on the isotopic composition of BSi in response to changing environmental conditions. Our main conclusion here is that *LGMbreezy* is apparently inconsistent with sedimentary redox-sensitive trace-metal records.

4.3 Model Uncertainties

Assessing the reliability of model projections is not straight-forward. This applies to both, climate models (Notz, 2015) and pelagic biogeochemical models (Löptien and Dietze, 2017). Our approach here is to highlight a choice of our simplifying *ad-hoc* assumptions which may potentially degrade our model results:

- DSi supply by rivers. In our simulations, all DSi supplied from the land into the ocean is homogeneously distributed over the oceans. The rationale behind this is the sparse information available on glacial-interglacial changes in river loads and the implicit assumption that horizontal transports act on much shorter timescales than the vertical transports. Among the (unintended) consequences is a glacial Arctic Ocean which is continuously flushed by isotopically light DSi in our model - even though - in reality, it was covered by ice and probably did not receive any river runoff at all.
- Isotopic fractionation during BSi dissolution. In our setup this is not to account for - an approach we share with the pioneering 3-dimensional modeling work of Wischmeyer et al. (2003), the box modeling work of Reynolds (2009), and the 3-dimensional modeling work of Gao et al. (2016). Our simulation of deep δ^{30}Si of DSi (see, Figure A.7) fits into this successive model development in that it features a realistic gradient in the deep waters of the Atlantic and Pacific Oceans.

©2020 American Geophysical Union. All rights reserved.

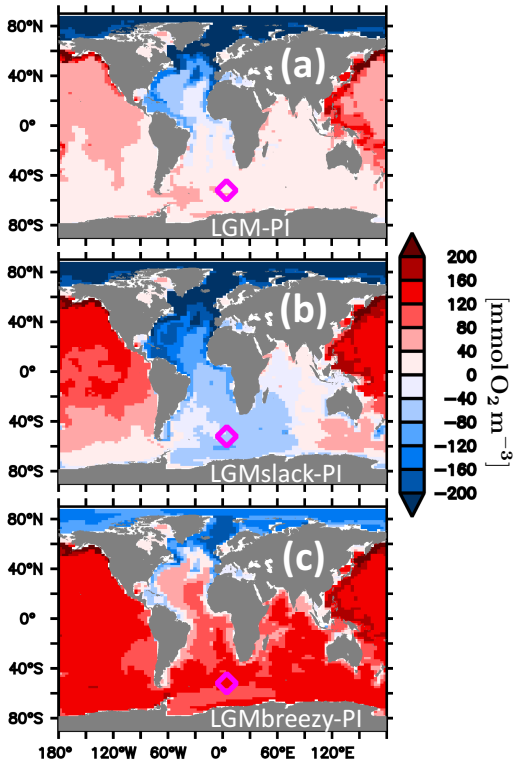

Figure 6. Simulated oxygen concentration at the bottom of the ocean relative to simulated preindustrial (PI) concentrations in units $mmol\,O2\,m^{-3}$. Panel (a), (b) and (c) refer to simulations *LGM, LGMslack* and *LGMbreezy*, respectively.

In comparison, the early work of Wischmeyer et al. (2003) failed to simulate a significant gradient (less than 0.1‰ difference), while Reynolds (2009) and Gao et al. (2016) reported a more realistic difference of 0.3‰ between the basins. Our model features 0.5‰ which is even closer to the data-constrained model estimate of 0.7‰ by Holzer and Brzezinski (2015) - arguably the most comprehensive estimate of today's δ^{30}Si of DSi distribution in the deep ocean. Further comparison with the Holzer and Brzezinski (2015) estimate, however, reveals that our simulated variance in the deep Pacific is apparently too low: while results by Holzer and Brzezinski (2015) suggest a range between 1.7‰ in the South and 1.1‰ up North, we find barely any variation in our simulation *PI*. According to Holzer and Brzezinski (2015) and Beucher et al. (2008) this deficiency of our model is linked to not accounting for isotopic fractionation during BSi dissolution.

- Diagenetic DSi release from sediments. The results presented here are based on a setup which neglects DSi release from sediments - even though it is known to be a significant agent in the world ocean silica cycle (Tréguer and De La Rocha, 2013). This simplification was necessitated by the computational burden that is associated with the long timescales of sedimentary processes. In order to test for robustness of our results, however, we followed up on a suggestions that surfaced during the review process. As described in more detail in Appendix B we decreased the export of BSi out of the lowermost wet model grid box in order to mimic the effects of diagenetic DSi release from the sediments. In summary: the thereby modified model version which is more complex in the sense that it contains more tunable model parameters performed better in terms of simulated DSi concentrations. As concerns the misfit between simulated glacial interglacial δ^{30}Si of BSi differ-

©2020 American Geophysical Union. All rights reserved.

ences, we find that our results as shown in Figure 3 a are robust (when compared with Figure B.2).

- Variable Si isotopic fractionation by diatoms. We apply the constant fractionation factor $\alpha_1 = 0.9989$ (De LaRocha et al., 1997; Gao et al., 2016) even though contradictory evidence suggests that fractionation factors vary among species (Sutton et al., 2013) and that Fe availability may modulate fractionation (Cavagna et al., 2011; Meyerink et al., 2017).

A problematic region where our model simulations deviate substantially from observations of δ^{30}Si of BSi is the eastern equatorial Pacific in Fig. 3 and 4. We speculate that this is associated with an unrealistic zonal circulation in our model which is apparently endemic to the current generation of coupled ocean circulation biogeochemical models (Dietze and Löptien, 2013; Getzlaff and Dietze, 2013).

In summary, we refer to a model that is capable of reproducing the effects of (preindustrial) circulation and isotopic fractionation during BSi production with a fidelity comparable to existing non data-assimilated 3-dimensional coupled ocean circulation biogeochemical models. Compared with the arguably most comprehensive data-assimilated model estimate of the present abyssal δ^{30} of DSi we miss an intra-basin variability in the Pacific Ocean that is probably linked to unaccounted isotopic fractionation during BSi dissolution.

5 Conclusions

We set out to simulate δ^{30}Si of BSi (such as opal) archived in oceanic sediments under modern climates (PI) and glacial conditions (LGM). Specifically, we implement and test several hypothesis which were suggested in the literature to explain the observed difference in δ^{30}Si of BSi between PI and LGM.

Our numerical experiments with an Earth System Model of intermediate complexity suggest that neither of the following processes effected glacial-interglacial changes in the isotopic composition of BSi is consistent with observations: (1) an overall cooling and substantial reduction of the meridional overturning circulation (our experiment *LGM*), (2) a decrease of Si:N quota in diatoms as potentially effected by increased air-sea iron fluxes (our experiment *LGMfe*), (3) decreasing winds (our experiment *LGMslack*) and (4) increasing or decreasing Si supply to the ocean (our experiments *LGMtrickle* and *LGMflush*).

Out of seven sensitivity experiments, only the simulation with increased winds (experiment *LGMbreezy*) and the simulation with a changed isotopic composition of river runoff (experiment *LGMlight*) reproduce the observed sign of change, specifically in the SO. The experiment with increasing winds (experiment *LGMbreezy*), however, fails to reproduce the magnitude of observed changes and is, furthermore, inconsistent with the Jaccard et al. (2016) estimate of dissolved near-bottom oxygen concentrations (based on redox-sensitive trace-metal records archived in the sediments in the Atlantic Sector of the SO). The experiment *LGMlight* is most consistent with observed changes in δ^{30}Si of BSi in terms of both, sign and magnitude. This confirms the suggestions by Frings et al. (2016) that changes in the isotopic composition of DSi supplied to the ocean (rather than changes in the internal oceanic cycling of DSi) triggered low glacial δ^{30}Si of BSi. Further, the estimated manifestation timescale of changes in δ^{30}Si of BSi range between several hundreds to 2500 years at the observational sites. This means that the respective signal should be detectable - despite a global turnover timescale of DSi, which is comparable to the period of glacial-interglacial cycles.

As a side aspect we find a simulated oceanic DSi inventory which is 10-20% lower during the Last Glacial Maximum than today. This is somewhat counterintuitive because

©2020 American Geophysical Union. All rights reserved.

simulated BSi production is also lower during the LGM which suggests that less BSi is sinking down to the oceanic sediment. More comprehensive analysis shows that this effect is outweighed by BSi dissolution rates that are also slowed down as a consequence of colder temperatures such that more BSi escapes dissolution prior to sedimentation in our model.

Caveats remain. A major problem of developing a Si module within the framework of an Earth System Model is the high computational cost associated with running test simulations to equilibrium. To this end, a turnover timescale of Si in the ocean of more than 10 000 years is a real handicap. Among the simplifications we chose in order to limit the number of test simulations was discarding the effect of fractionation during BSi dissolution. According to Holzer and Brzezinski (2015) and Beucher et al. (2008) this may be the reason why our model does not reproduce observed variations of δ^{30}Si of DSi within the Pacific. Further - substantial - uncertainty is added by the generic problem of constraining global biogeochemical ocean models (Löptien and Dietze (2015); Löptien and Dietze (2017); Löptien and Dietze (2019)).

A Model Assessment

The UVic ESCM reference version we use for *LGM* and *PI* has been described and assessed by Brennan et al. (2012). We left this base module unchanged. In the following we refer to our extension adding an Si-cycle (which does not feedback onto the original modules) in the following.

Figure A.1 shows the modern climate (PI) simulated DSi concentrations at the surface and at depth compared to observations (Garcia et al., 2010). A comparison of panel (a) and (c) suggests that the simulated DSi concentrations are somewhat too high at the surface, specifically in the tropics and the southern part of the Southern Ocean. At the same time, DSi concentrations are too low at the bottom, specifically in the northern Pacific (panel (b) and (d)). These deviations are also visible in the global mean profiles in Fig. A.2.

Table A.1. Comparison between observations (OBS) and preindustrial simulation (*PI*). Temp., Sal., std., RMS, corr. coeff. and var refer to temperature, salinity, standard deviation, root mean square error between PI and OBS, and variance, respectively. $\delta^{30}DSi$ refers to surface values. The origin of observations is documented in Section 2.1.

variable	unit	std. OBS	std. *PI*	bias (*PI*-OBS)	RMS	corr. coeff.	var(*PIref*)/ var(OBS)
Temp.	$°C$	6.5	6.6	0.6	1.4	0.98	103%
Sal.	PSU	0.6	0.5	0.03	0.3	0.85	70%
PO_4	$mmol\,P\,m^{-3}$	0.83	0.77	-0.03	0.3	0.94	86%
O_2	$mmol\,O_2\,m^{-3}$	77	75	2	28	0.93	95%
DSi	$mmol\,Si\,m^{-3}$	54	40	11	30	0.84	54%
$\delta^{30}DSi$	‰	0.62	0.48	0.57	0.56	0.51	60%

We suspect that these differences are both the result of our choice of parameters (possibly an underestimated opal sinking velocity and an underestimated molecular DSi to phosphate stoichiometric ratio or an underestimated BSi production rate) as well as being caused by rather coarse spatial resolution of the ocean module which is known to retard ocean transports (e.g. Getzlaff and Dietze, 2013). An additional cause for model

©2020 American Geophysical Union. All rights reserved.

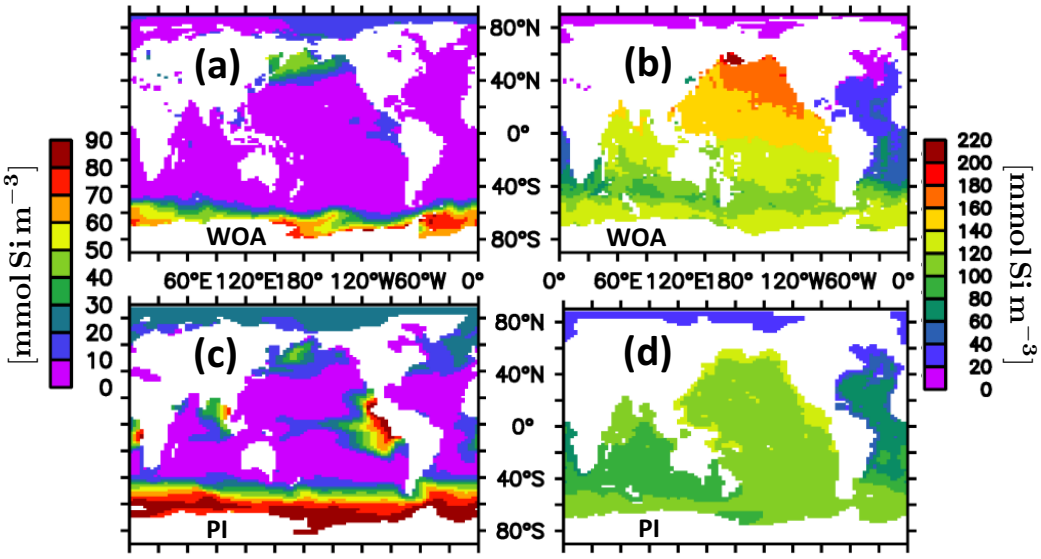

Figure A.1. Surface and deep (2000 m to bottom average) DSi concentrations in units $mmol\,Si/m^3$. (a) and (b) refer to surface and abyssal observations (Garcia et al., 2010), respectively. (c) and (d) refer to simulated preindustrial (PI) surface and abyssal concentrations, respectively.

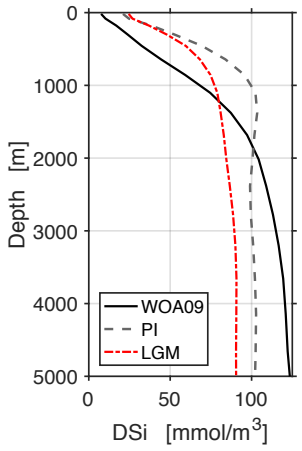

Figure A.2. Zonally and meridionally averaged vertical profile of DSi concentrations in units $mmol\,Si/m^3$. The black, grey dashed, and red dot-dashed lines refer to observations (black line, Garcia et al., 2010), preindustrial simulation, and Last Glacial Maximum simulation, respectively.

data misfits of DSi concentrations is followed up in the Appendix B where we added a brief investigation into the effect of diagentic DSi release from sediments.

Figure A.3 depicts the zonally averaged export of DSi. While the above mentioned biases map also onto this metric, the major features are, nevertheless, captured. Specifically the trapping of DSi in the SO, high values in the tropics and a large drop in the Arctic are clearly visible. Not well captured are, however, the mid latitudes in the northern hemisphere where the simulated export is underestimated. Further, the transition

©2020 American Geophysical Union. All rights reserved.

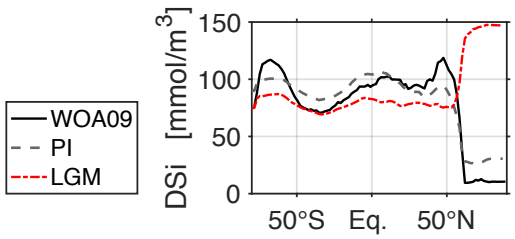

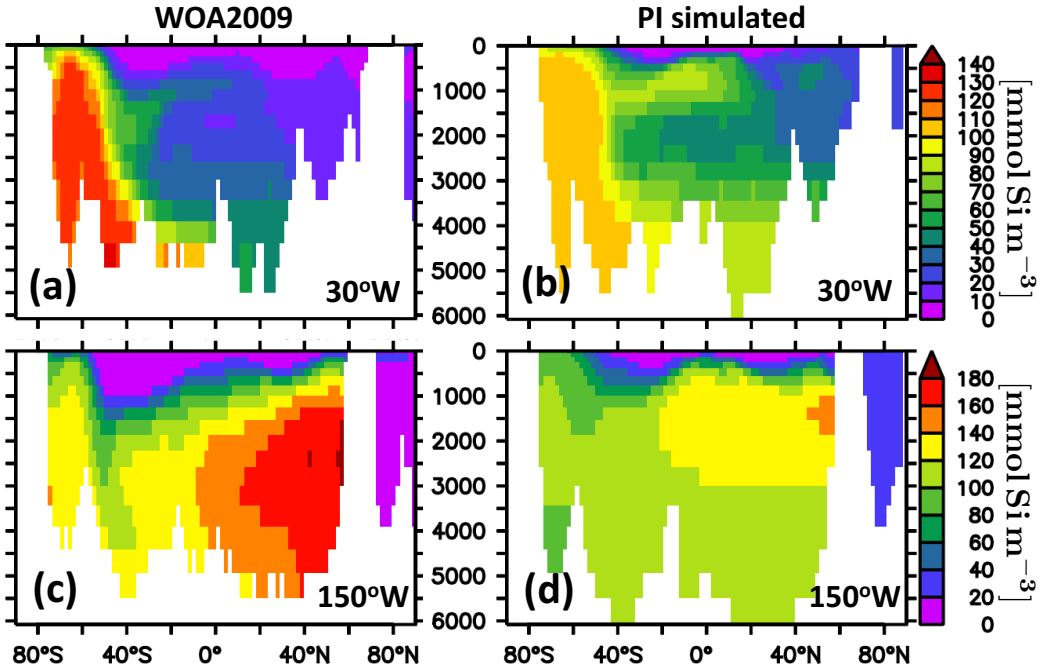

Figure A.4. Meridional sections over depth (in m) of DSi in units $mmol\,Si\,m^{-3}$. Panel (a) and (c) refer to observations (Garcia et al., 2010) and panel (b) and (d) to the preindustrial simulation.

zone to the SO is not as sharp as observed and DSi values in the Arctic are somewhat overestimated.

The Figures A.4 and A.5 show meridional sections of both, simulated DSi and phosphate in comparison to the observations. This allows for a continuative exploration of the reasons for model-data mismatches with respect to DSI : the section through the Atlantic (at 30°W) shows simulated DSi concentrations that are generally underestimated while phosphate seems in better agreement with the observations in that respect. In the SO, however, both variables are biased - and the biases oppose one another: in terms of SO nutrient trapping, simulated phosphate is trapped more efficiently than indicated by the observations. This is mirrored by the low bias of simulated SO dissolved oxygen concentrations (Figure A.6) indicating an overestimation of accumulated remineralization. This is in contrast to simulated DSi concentrations, where the simulated SO nutrient trapping is too weak. With one nutrient biased high and the other nutrient biased

©2020 American Geophysical Union. All rights reserved.

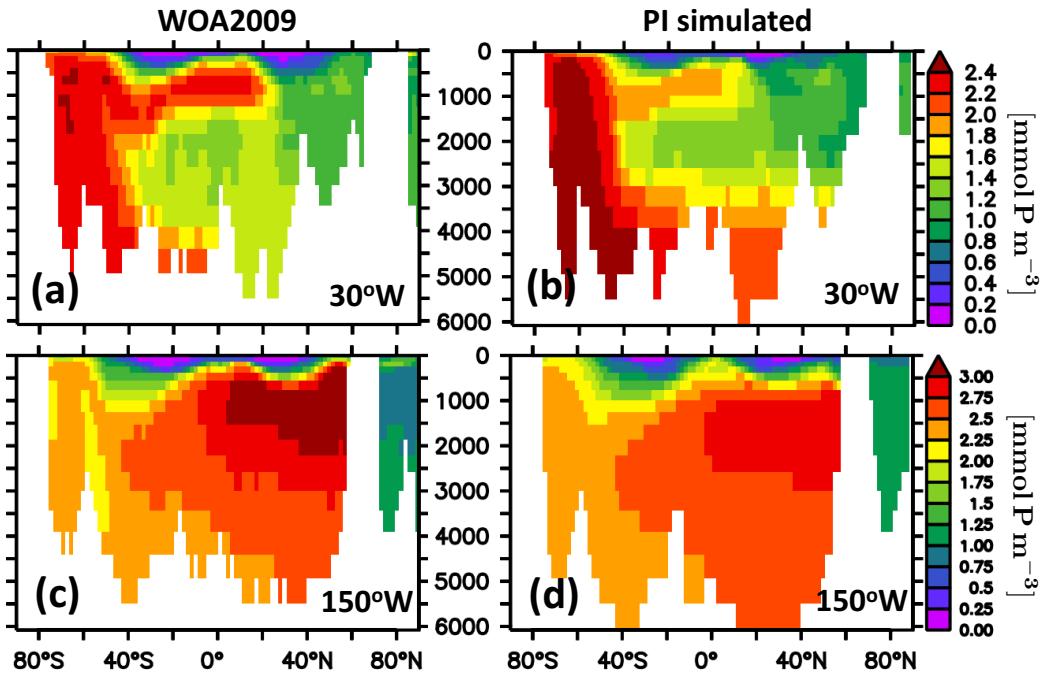

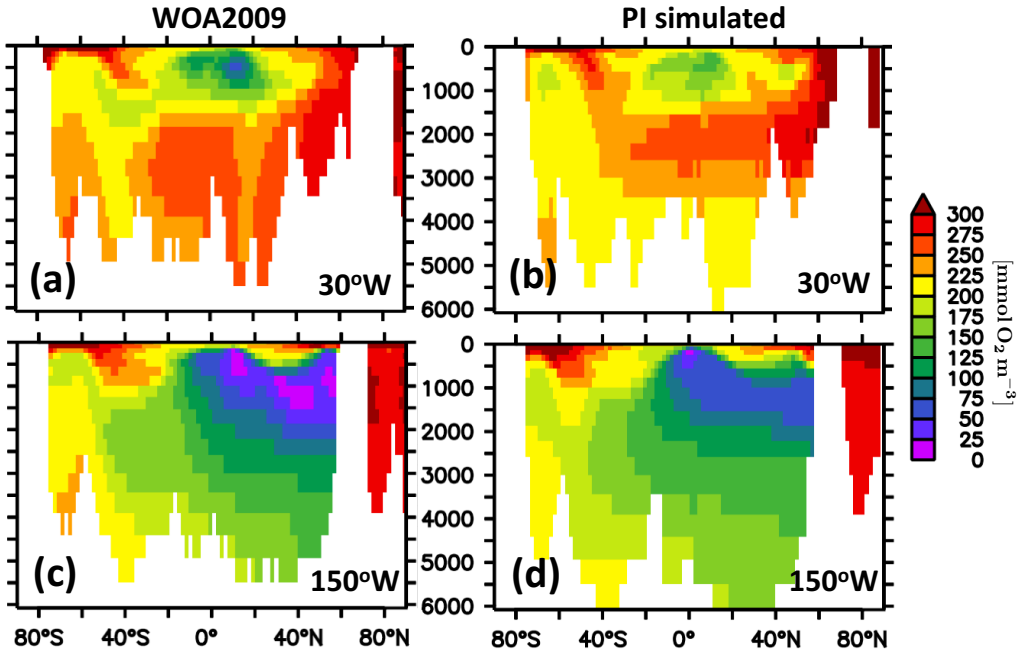

Figure A.6. Meridional sections over depth (in m) of dissolved O_2 in units $mmol\,O_2\,m^{-3}$. Panel (a) and (c) refer to observations (Garcia et al., 2010) and panel (b) and (d) to the preindustrial simulation.

©2020 American Geophysical Union. All rights reserved.

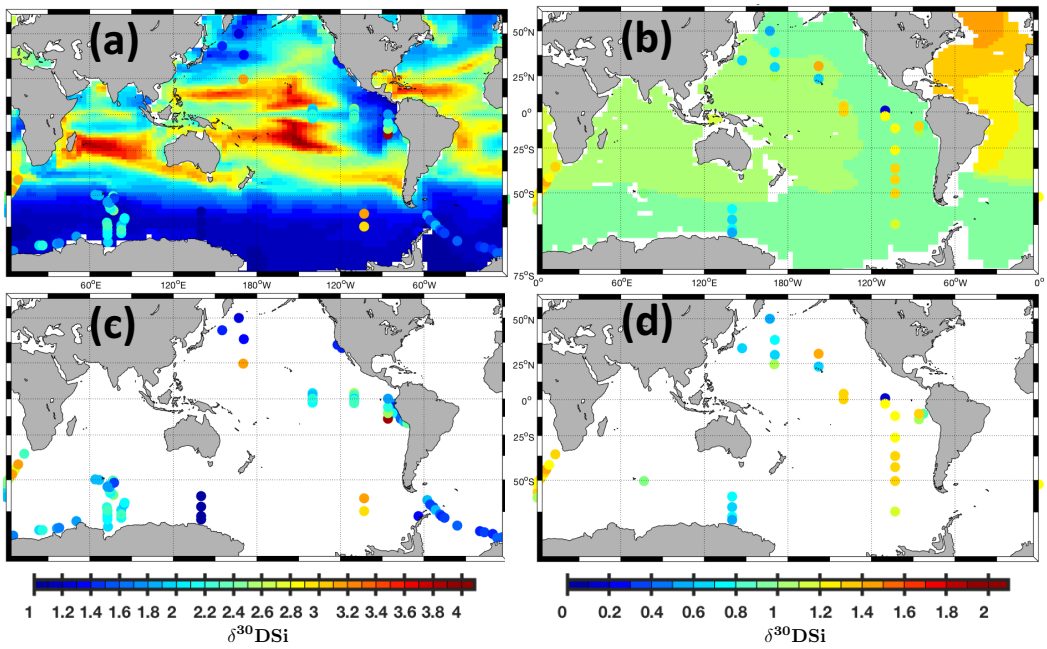

Figure A.7. $\delta^{30}DSi$ at the surface (50 m, panel (a) & (c)) and at depth (2000 m, panel (b) & (d)) in units ‰. The colored blobs denote those observations (see Section 2.1) within 0-100 m (1500-2500 m) that are closest to the nominal depth of 50 m (2000 m). The background color in panel (a) and (b) refers to simulation PI. Panel (c) and (d) show respective observations only to facilitate their recognition.

low it seems unlikely that a deficient circulation is the cause for these biases (although this can not be ruled out). Hence, the SO nutrient trapping apparently relates strongly to the biogeochemical model parameters. One conclusion from this may be that the biogeochemical model is better tuned with respect to phosphate than to DSi. This is to be expected because of the wider use of the phosphate-based biogeochemical model and the much shorter equilibration time scales for phosphate which facilitate the respective tuning to observations. In the Pacific, however, the situation differs, and subsurface maxima in the northern hemisphere (except the Arctic) are too low for both phosphate and DSi. Following our reasoning above this may be indicative for flaws in the ocean circulation module. Please note, however, that the attribution of flaws in model behavior to respective processes is challenging and may even be impossible given the current set of observations (e.g. Löptien and Dietze, 2019).

Table A.1 provides a quantitative estimate of how our DSi/BSi module compares against the underlying biogeochemical and ocean circulation module of Brennan et al. (2012). The simulated temperature variance is overestimated by 3% and the temperature bias is 0.6 K, corresponding to 9% relative to the standard deviation in the observations. The respective bias to standard deviation of salinity is with 0.03 even smaller (5% relative to the standard deviation in the observations). Simulated phosphate concentrations are, surprisingly, even closer to observations than simulated salinities (note that this does also apply to simulated dissolved oxygen concentrations): the bias to standard deviation ratio is smaller (4%) and the simulated variance covers 86% of observed levels (versus 70% for salinity). Given that the salinity distribution directly affects ocean circulation via density driven pressure gradients, it is remarkable that the misfit in this active physical property can be much larger than the misfit of the rather passive (in terms

©2020 American Geophysical Union. All rights reserved.

of their effect on circulation) phosphate whose distribution is directly shaped by oceanic circulation. This may be an indication that the biogeochemical module of Brennan et al. (2012) has been "overly successfully" tuned to a flawed physics (a process illustrated by Löptien and Dietze, 2019). In contrast, the simulated DSi features the largest deviations among the metrics reviewed here. The simulation features a variance corresponding to 54% of observed levels and the simulated bias is 21% relative to the observed standard deviation. The correlation of simulated DSi concentrations with observations is, however, rather good in the sense that it is very similar to that of salinity (0.84 versus 0.85).

Fig. A.7 shows our simulated preindustrial δ^{30}DSi distribution. The sparseness of observational data with often times puzzling inhomogeneities illustrates the Hendry and Brzezinski (2014) conclusion that the δ^{30}DSi data set is "... inadequate to evaluate mechanisms leading to even the first-order distribution of isotopes of Si in the global ocean". Also we are urged to compare point observations to large scale averages, resolved by the model. The relatively low correlation of 0.51 between model and observations has thus to be considered with some caution. Please note that a clearer picture seems to be found for the more abrupt events of the deglacial, leading to the Silic Acid Ventilation Hypothesis of Hendry and Brzezinski (2014).

B Silica dissolution rates, temperature and diagenetic DSi release from sediments

One of the major processes at work in our simulations is a reduced glacial oceanic DSi inventory (relative to preindustrial). Lower glacial temperatures slow down BSi dissolution such that more BSi sinks into the sediments where it is lost forever in our model. In turn, the overall reduced availability of DSi invokes more DSi limitation which manifests itself in a glacial tendency towards higher δ^{30}DSi which is apparently inconsistent with the observed tendency to generally lower glacial δ^{30}DSi.

During the review process of an earlier version of this manuscript the following concerns were put forward: our model does not account for diagenetic release of DSi from sediments even though it is known to be substantial (e.g., Tréguer and De La Rocha, 2013). Hence, our model neglects a process that retains Si in the ocean. Even so, our simulated DSi inventory is close to observations - because we adjusted the silica dissolution rate accordingly (Figure 1). This procedure yielded a functional dependency of silica dissolution and temperature which is at the lower end of data compiled by Kamatani (1982) and shown in Figure 2. In the following we will discuss if this may have flawed our results.

We integrate an additional set of model simulations dubbed PI^* and LGM^* for 10000 years (starting from the spunup simulations PI and LGM). PI^* and LGM^* are identical to PI and LGM except for: (1) We use the Gao et al. (2016) opal dissolution rate $A = 333^{-1} day^{-1}$ which yields a functional dependency of silica dissolution and temperature which is at the upper end of data compiled by Kamatani (1982) and shown in Figure 2. (2) We reduce the sinking velocity of BSi out of the lowermost wet model grid box from $10\,\mathrm{m\,day^{-1}}$ down to $0.5\,\mathrm{m\,day^{-1}}$ in order to mimic the effect of diagenetic DSi release (or, more specifically, the increased residence time of Si at the bottom of the water column).

Integration of PI^* for 10000 years resulted in a fairly equilibrated DSi inventory close to observations ($\approx$ 3% less than Garcia et al., 2010). The DSi concentrations of PI^* are more realistic than in the reference version PI. In terms of route mean square error the misfit drops substantially from 30 (Table A.1) down to $15\,mmol\,Si\,m^{-3}$ (Table B.1). The increase in realism is confirmed by visually inspecting Figure B.2 versus Figure A.4.

©2020 American Geophysical Union. All rights reserved.

In terms of $\delta^{30}DSi$ we find that PI^* features a variance more similar to observations compared to PI (93% versus 60%; Table B.1 versus Table A.1). The correlation does, however, not improve probably because we do not account for isotopic fractionation during BSi dissolution (see discussion in Section 4.3).

In summary, PI^* features a more realistic DSi distribution, more realistic levels of $\delta^{30}DSi$ variance and a (rough) representation of diagenetic DSi release from the sediments. Further, PI^* features a functional dependency of silica dissolution and temperature that is the upper end of data compiled by Kamatani (1982) - as opposed to PI which features a functional dependency that is at the lower end. Even so the glacial-interglacial sensitivity of δ^{30}Si of BSi is apparently robust: Figure B.2 shows the LGM^* - PI^* difference that is similar to the respective LGM - PI difference in Figure 3 in that the simulated changes are opposing the observational evidence.

Table B.1. Comparison between observations (OBS) and preindustrial simulation (PI^*). std., RMS, corr. coeff., var refer to standard deviation, root mean square error between simulation PI^* and OBS, and variance, respectively. $\delta^{30}DSi$ refers to surface values. The origin of observations is documented in Section 2.1.

variable	unit	std. OBS	std. PI	bias (PI-OBS)	RMS	corr. coeff.	var($PIref$)/ var(OBS)
DSi	$mmol\,Si\,m^{-3}$	54	49	-1.2	15	0.96	83%
$\delta^{30}DSi$	‰	0.62	0.60	-0.29	0.58	0.54	93%

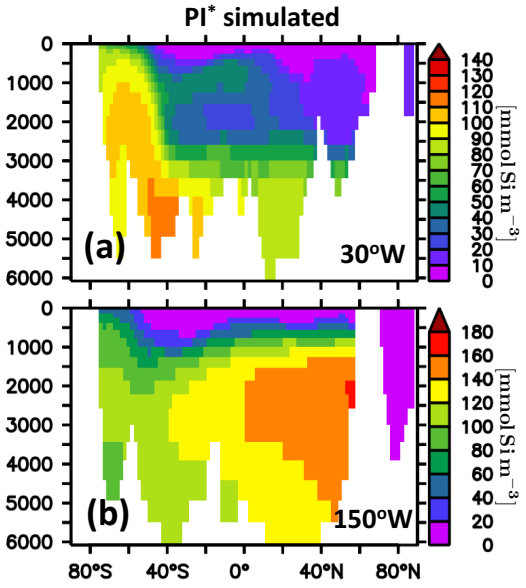

Figure B.1. Meridional sections over depth (in m) of DSi in units $mmol\,Si\,m^{-3}$. Panel (a) and (b) refer to simulation PI^* that applies the Gao et al. (2016) opal dissolution rate $A = 333^{-1} day^{-1}$ and that mimics diagenetic release of DSi from sediments by reducing the sinking velocity of BSi from $10\,m\,day^{-1}$ to $0.5\,m\,day^{-1}$ in the lowermost wet model grid box.

©2020 American Geophysical Union. All rights reserved.

Accepted Article

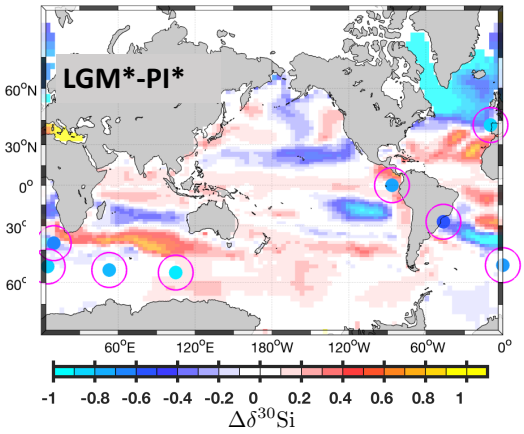

Figure B.2. Difference in simulated LGM δ^{30}Si of BSi relative to the preindustrial simulation *PI** as deposited to sediments in units ‰. The difference to Figure 3 (a) ist that both *LGM** and *PI** refer to simulations that apply the Gao et al. (2016) opal dissolution rate $A = 333^{-1} day^{-1}$ and that mimic diagenetic release of DSi from sediments by reducing the sinking velocity of BSi from $10\,m\,day^{-1}$ to $0.5\,m\,day^{-1}$ in the lowermost wet model grid box.

Acknowledgments

H. D. and U. L. acknowledge funding by Deutsche Forschungsgemeinschaft (DFG) in the framework of the priority program *Antarctic Research with comparative investigations in Arctic ice areas SPP 1158* by grant no. *SCHN 762/5-1*. We acknowledge discussions with Mark Holzer and Katrin Meissner. Katrin Meissner provided the model configuration (to which we added the Si cycle) by sharing code and forcing files. Fruitful discussion with Richard Matear and Andrew Lenton were made possible by DFG grant no. *DI 1665/6-1* and *LO 1377/5-1*. A number of very good review papers eased the entry of H. D. and U. L. into the field. We are grateful to each and everyone sharing observational data. Data is available through Locarnini et al. 2010, Antonov et al. 2010, Garcia et al. 2010, Beucher et al. 2008, Cardinal et al. 2005, De La Rocha et al. 2011, de Souza et al. 2012, Ehlert et al. 2012, Fripiat et al. 2011, Grasse et al. 2013, Reynolds et al. 2006, Frings et al. 2016, Brzezinski et al. 2002, De La Rocha et al. 1997, De La Rocha et al. 1998, De La Rocha et al. 2011, Ehlert et al. 2013, Ellwood et al. 2010, Hendry et al. 2012, Hendry et al. 2016, Horn et al. 2011, and Pichevin et al. 2009. The model configurations and output is archived at `https://zenodo.org/record/3959258#.XxsN6B1CRTY` under doi:10.5281/zenodo.3959257. We thank one anonymous reviewer, Christoph Voelker and the editorial team for their constructive work and effort!

©2020 American Geophysical Union. All rights reserved.

Accepted Article

References

Antonov, J. I., Seidov, D., Boyer, T. P., Locarnini, R. A., Mishonov, A. V., Garcia, H. E., Baranova, O. K., Zweng, M. M., and Johnson, D. R., (2010). World Ocean Atlas 2009, Volume 2: Salinity. S. Levitus, Ed. NOAA Atlas NESDIS 69, U.S. Government Priniting Office, Washington, D.C., 184pp.

Basile-Doelsch, I., (2006). Si stable isotopes in the Earth's surface: A review. Journal of Geochemical Exploration, 88, 252–256, doi:10.1016/j.gexplo.2005.08.050.

Bauer, P., Thorpe, A., and Brunet, G., (2015). The quet revolution of numerical weather prediction. Nature, 525, 7567, 47–55, doi:10.1038/nature14956.

Beucher, C. P., Brzezinski, M. A., and Jones, J. L., (2008). Sources and biological fractionation of Silicon isotopes in the Eastern Equatorial Pacific. Geochimica et Cosmochimica Acta, 72, 3063–3073, doi:10.1016/j.gca.2008.04.021.

Beucher, C. P., Brzezinski, M. A., and Jones, J. L., (2011). Mechanisms controlling silicon isotope distribution in the Eastern Equatorial Pacific. Geochimica et Cosmochimica Acta, 75, 4286–4294, doi:0.1016/j.gca.2011.05.024.

Braconnot, P., Harrison, S. P., Kageyama, M., Bartlein, P. J., Masson-Delmotte, V., Abe-Ouchi, A., Otto-Bliesner, B., and Zhao, Y., (2012). Evaluation of climate models using palaeoclimatic data. Nature Climate Change, 2, 417–424, doi:10.1038/NCLIMATE1456.

Brennan, C. E., Weaver, A. J., Eby, M., and Meissner, K. J., (2012). Modelling Oxygen Isotopes in the University of Victoria Earth System Climate Model for Preindustrial and Last Glacial Maximum Conditions. Atmosphere-Ocean, 50, 4, 447–465, doi:10.1080/07055900.2012.707611.

Brzezinski, M. A., Pride, C. J., Franck, V. M., Sigman, D. M., Sarmiento, J. L., Matsumoto, K., Gruber, N., Rau, G. H., and Coale, K. H., (2002). A switch from $Si(OH)_4$ to NO_3^- depletion in the glacial Southern Ocean. Geophysical Reserach Letters, 29, 12, 1564, doi:10.1029/2001GL014349.

Cardinal, D., Alleman, L. Y., Dehairs, F., Savoye, N., Trull, T. W., and André, L., (2005). Relevance of silicon isotopes to Si-nutrient utilization and Si-source assessment in Antarctic waters. Global Biogeochemical Cycles,19, GB2007, doi:10.1029/2004GB002364.

Cavagna, A.-J., Fripiat, F., Dehairs, F., Wolf-Gladrow, D., Cisewski, B., Savoye, N., André, L., and Cardinal, D., (2011). Silicon uptake and supply during a Southern Ocean iron fertilization experiment (EIFEX) tracked by Si isotopes. Limnology and Oceanography, 56, 1, 147–160, doi:10.4319/lo.2011.56.1.0147.

Closset, I., Cardinal, D., Rembauville, M., Thil, F., and Blain, S., (2016). Unveiling the Si cycle using isotopes in an iron-fertilized zone of the Southern Ocean: from mixed-layer supply to export. Biogeosciences, 13, 6049–6066, doi:10.5194/bg-13-6049-2016.

Coplen, T. B., Hopple, J. A., Böhlke, J. K., Peiser, H. S., Rieder, S. E., Krouse, H. R., Rosman, K. J. R., Ding, T., Vocke, Jr., R. D., Révész, K. M., Lamberty, A., Taylor, P., and De Bièvre, (2002). Compilation of Minimum and Maximum Isotope Ratios of Selected Elements in Naturally Occurring Terrestrial Materials and Reagents, Water-Resources Investigation Report, 01-4222, 1–110, U.S. Department of the Interior and U.S. Geological Survey, Reston Virginia.

De La Rocha, C. L., Brzezinski, M. A., and De Niro, M. J., (1998). Fractionation of silicon isotopes by marine diatoms during biogenic silica formation. Geochimica et Cosmochimica Acta, 61, 23, 5051–5056, doi:10.1016/S0016-7037(97)00300-1.

De La Rocha, C. L., Brzezinski, M. A., De Niro, M. J., and Shemesh, A., (1998). Silicon-isotope composition of diatoms as an indicator of past oceanic change. Nature, 395, 680–683, doi:10.1038/27174.

De La Rocha, C. L., Bescont, P., Croguennoc, A., Ponzevera, E., (2011). The silicon isotopic composition of surface waters in the Atlantic and Indian sectors of the Southern Ocean. Geochimica et Cosmochimica Acta, 75,5283–5295,

©2020 American Geophysical Union. All rights reserved.

doi:10.1016/j.gca.2011.06.028.

de Souza, G. F., Reynolds, B. C., Johnson, G. C., Bullister, J. L., and Bourdon, B., (2012a). Silicon stable isotope distribution traces Southern Ocean export of Si to the South Pacific thermocline. Biogeosciences, 9, 4199–4213, doi:10.5194/bg-9-4199-2012.

de Souza, G. F., Reynolds, B. C., Rickli, J., Frank, M., Saito, M. A., Gerringa, L. J. A., and Bourdon, B., (2012). Southern Ocean control of silicon stable isotope distribution in the deep Atlantic Ocean. Global Biogeochemical Cycles, 26, GB2035, doi:10.1029/2011GB004141.

Dietze, H., and Löptien, U., (2013). Revisiting "nutrient trapping" in global coupled biogeochemical ocean circulation models. Global Biogeochemical Cycles, 27, 265–284, doi:10.1002/gbc.20029.

Ehlert C., Grasse, P., Mollier-Vogel, E., Böschen, T., Franz, J., de Souza, G. F., Reynolds, B. C., Stramma, L., and Frank, M., (2012). Factors controlling the silicon isotope distribution in waters and surface sediments of the Peruvian coastal upwelling. Geochimica et Cosmochimica Acta 99, 128–145, doi:10.1016/j.gca.2012.09.038.

Ehlert, C., Grasse, P., and Frank, M., (2013). Changes in silicate utilisation and upwelling intensity off Peru since the Last Glacial Maximum - insights from silicon and neodymium isotopes. Quaternary Science Reviews, 72, 18–35, doi:10.1016/j.quascirev.2013.04.013.

Ellwood, M. J., Wille, M., and Maher, W., (2010). Glacial Silicic Acid Concentration in the Southern Ocean. Science, 330, 6007, 1088–1091, doi:10.1126/science.1194614.

Franck, V. M., Brzezinski, M. A., Coale, K. H., and Nelson, D. M., (2000). Iron and silicic acid concentrations regulate Si uptake north and south of the Polar Frontal Zone in the Pacific Sector of the Southern Ocean. Deep-Sea Research Part II, 47, 3315–3338, doi:10.1016/S0967-0645(00)00070-9.

Frings, P. J., Clymans, W., Fontorbe, G., De La Roche, C. L., and Conley, D. J., (2016). The continental Si cycle and its impact on the ocean Si isotope budget. Chemical Geology, 425, 12–36, doi:10.1016/j.chemgeo.2016.01.020.

Fripiat, F., Cavagna, A.-J., Dehairs, F., Speich, S., André, L., and Cardinal, D., (2011). Silicon pool dynamics and biogenic silica export in the Southern Ocean inferred from Si-isotopes. Ocean Science, 7, 533–547, doi:10.5194/os-7-533-2011.

Fripiat, F., Cavagnam A.-J., Savoye, N., Dehairs, F., André, L., and Cardinal, D., (2011). Isotopic constraints on the Si-biogeochemical cycle of the Antarctic Zone in the Kerguelen area (KEOPS). Marine Chemistry, 123, 11-22, doi:10.1016/j.marchem.2010.08.005.

Fripiat, F., Cavagna, A.-J., Dehairs, F., de Brauwere, A., André, L., and Cardinal, D., (2012). Processes controlling the Si-isotopic composition in the Southern Ocean and application for paleoceanography. Biogeosciences, 9, 2443–2457, doi:10.5194/bg-9-2443-2012.

Gao, S., Wolf-Gladrow, D. A., and Völker, C., (2016). Simulating the modern δ^{30}Si distribution in the oceans and in marine sediments. Global Biogeochemical Cycles, 30, 120–133, doi:10.1002/2015GB005189.

Garcia, H. E., Locarnini, R. A., Boyer, T. P., and Antonov, J. I., Baranova, O. K., Zweng, M. M., and Johnson, D. R., (2010). World Ocean Atlas 2009, Volume 3: Dissolved Oxygen, Apparent Oxygen Utilization, and Oxygen Saturation. S. Levitus, Ed. NOAA Atlas NESDIS 70, U.S. Government Printing Office, Washington, D.C., 344 pp.

Garcia, H. E., Locarnini, R. A., Boyer, T. P., and Antonov, J. I., (2010). World Ocean Atlas 2009, Volume 4: Nutrients (phosphate, nitrate, silicate). S. Levitus, Ed. NOAA Atlas NESDIS 71, U.S. Government Printing Office, Washington, D.C., 398 pp.

©2020 American Geophysical Union. All rights reserved.

Grasse, P., Ehlert, C., and Frank, M., (2013). The influence of water mass mixing on the dissolved Si isotope composition in the Eastern Equatorial Pacific. Earth and Planetary Science Letters, 380, 60–71, doi:10.1016/j.epsl.2013.07.033.

Getzlaff, J., and Dietze, H., (2013). Effects of increased isopycnal diffusivity mimicking the unresolved equatorial intermediate current system in an earth system climate model. Geophysical Research Letters, 40, 10, doi:10.1002/grl.50419.

Georg, R. B., West, A. J., Basu, A. R., and Halliday, A. N., (2009). Silicon fluxes and isotope composition of direct groundwater discharge into the Bay of Bengal and the effect on the global ocean silicon isotope budget. Earth and Planetary Science Letters, 283, 67–74, doi:10.1016/j.epsl.2009.03.041.

Hawkins, J. R., Hatton, J. E., Hendry, K. R., de Souza, G. F., Wadham, J. L., Ivanovic, R., Kohler, T. J., Stibal, M., Beaton, A., Lamarche-Gagnon, G., Tedstone, A., Hain, M. P., Bagshaw, E., Pike, J., and Tranter, M., (2018). The silicon cycle impacted by past ice sheets. Nature Communicationa, 9, 3210, doi:10.1038/s41467-018-05689-1.

Hendry, K. R., and Brzezinski, M. A., (2014). Using silicon isotopes to understand the role of the Southern Ocean in modern and ancient biogeochemistry and climate. Quaternary Science Reviews, 89, 13–26, doi:10.1016/j.quascirev.2014.01.019.

Hendry, K. R., Gong, X., Knorr, G., Pike, J., and Hall, I. R., (2016). Deglacial diatom production in the tropical North Atlantic driven by enhanced silic acid supply. Earth and Planetary Science Letters, 438, 122–129, doi:10.1016/j.epsl.2016.01.016.

Hendry, K. R., Robinson, L. F., Meredith, M. P., Mulitza, S., Chiessi, C. M., and Arz, H., (2012). Abrupt changes in high-latitude nutrient supply to the Atlantic during the last glacial cycle. Geology, 40, 2, 123–126, doi:10.1130/G32779.1.

Holzer, M., and Brzezinski, M. A., (2016). Controls on the silicon isotope distribution in the ocean: New diagnostics from a data-constrained model. Global Biogeochemical Cycles, 29, 267–287, doi:10.1002/2014GB004967.

Horn, M., Beucher, C. P., Robinson, R. S., and Brzezinski, M. A., (2011). Southern ocean nitrogen and silicon dynamics during the last deglaciation. Earth and Planetary Science Letters 310, 334–339, doi:10.1016/j.epsl.2011.08.016.

Hülse, D., Arndt, S., Wilson, J. D., Munhoven, G., and Ridgwell, A., (2017). Understanding the causes and consequences of past marine carbon cycling variability through models. Earth-Science Reviews 171, 349–382, doi:10.1016/j.earscirev.2017.06.004.

Hutchins, D. A., and Bruland, K. W., (1998). Iron-limited diatom growth and Si:N uptake ratios in a coastal upwelling regime. Nature, 393, 561–564, doi:10.1038/31203.

Jaccard, S. L., and Galbraith, E. D., (2011). Large climate-driven changes of oceanic oxygen concentrations during the last deglacation. Nature Geoscience, 5, 151–156, doi:10.1038/NGEO1352.

Jaccard, S. L., Galbraith, E. D., Martínez-García, A., and Anderson, R. F., (2016). Covariation of deep Southern Ocean oxygenations and atmospheric CO_2 through the last ice age. Nature, 530, doi:10.1038/nature16514.

Kamatani, A., (1992). Dissolution Rates of Silica from Diatoms Decomposition at Various Temperatures. Marine Biology, 68, 91–96.

Knutti, R., Furrer, R., Tebaldi, C., Cermak, J., and Meehl, G. A., (2009). Challenges in Combining Projections from Multiple Climate Models. Journal of Climate, 2739–2758, doi:10.1175/2009JCLI3361.1.

Kohlfeld, K. E., Graham, R. M., de Boer, A. M., Sime, L. C., Wolff, E. W., Le Quéré, C., and Bopp, L., (2013). Southern Hemisphere westerly wind changes during the Last Glacial Maximum: paleo-data synthesis. Quaternary Science Reviews, 68, 76–95, doi:10.1016/j.quascirev.2013.01.017.

©2020 American Geophysical Union. All rights reserved.

Kriest, I., and Oschlies, A., (2008). On the treatment of particulate organic matter sinking in large-scale models of marine biogeochemical cycles. Biogeosciences, 5, 55-72, doi:10.5194/bg-5-55-2008.

Lagarias, J. C., Reeds, J. A., Wright, M. H., and Wright, P. E., (1998). Covergence Properties of the Nelder–Mead Simplex Method in Low Dimensions. SIAM Journal on Optimization, 9,1,112–147, doi:10.1137/S1052623496303470.

Locarnini, R. A., Mishonov, A. V., Antonov, J. I., Boyer, T. P., Garcia, H. E., Baranova, O. K., Zweng, M. M., and Johnson, D. R., (2010). World Ocean Atlas 2009, Volume 1: Temperature. S. Levitus, Ed. NOAA Atlas NESDIS 68, U.S. Government Printing Office, Washington, D.C., 184 pp.

Löptien, U., and Dietze, H., (2015). Constraining parameters in marine pelagic ecosystem models - is it actually feasible with typical observations of standing stocks? Ocean Science, 11, 4, 573–590, doi:10.5194/os-11-573-2015.

Löptien, U., and Dietze, H., (2017). Effects of parameter indeterminancy in pelagic biogeochemical modules of Earth System Models on projections into a warming future: The scale of the problem. Global Biogeochemical Cycles, 31, 7, 1155–1172, doi:10.1002/2017GB005690.

Löptien, U., and Dietze, H., (2019). Reciprocal bias compensation and ensuing uncertainties in model-based climate projections: pelagic biogeochemistry versus ocean mixing. Biogeosciences, 16, 1865–1881, doi:10.5194/bg-16-1865-2019.

Margo Project Members, (2009). Constraints on the magnitude and patterns of ocean cooling at the Last Glacial Maximum. Nature Geoscience, 2, 127–132, doi:10.1038/NGEO411.

Matsumoto, K., Chase, Z., and Kohfeld, K., (2014). Different mechanisms of silicic acid leakage and their biogeochemical consequences. Paleoceanography, 29, doi:10.1002/2013PA002588.

Matsumoto, K., Sarmiento, J. L., and Brzezinski, M. A., (2002). Silicic acid leakage from the Southern Ocean: A possible explanation for glacial atmospheric pCO_2. Global Biogeochemical Cycles, 16, 3, 1031, doi:10.1029/2001GB001442.

Matsumoto, K., and Sarmiento, J. L., (2008). A corollary to the silic acid leakage hypothesis. Paleoceanography, 23, PA2203, doi:10.1029/2007PA001515.

McGee, D., Broecker, W. S., and Winckler, G., (2010). Gustiness: The driver of glacial dustiness? Quaternary Science Reviews, 29, 17-18, 2340–2350, doi:10.1016/j.quascirev.2010.06.009.

Meyerink, S., Ellwood, M. J., Maher, W., and Strzepek, R., (2017). Iron Availability Influences Silicon Isotope Fractionation in Two Southern Ocean Diatoms (Proboscia inermis and Eucampia antarctica) and a Coastal Diatom (Thalassiosira pseudonana). Frontiers in Marine Science, 4, 217, doi:10.3389/fmars.2017.00217.

Moore, J. K., Fu, W., Primeau, F., Britten, G. L., Lindsay, K., Long, M., Doney, S., Mahowald, N., Hoffman, F., and Randerson, J., (2018). Sustained climate warming drives declining marine biological productivity. Science, 359, 6380, 1139–1143, doi:10.1126/science.aao6379.

Notz, D., (2015). How well must climate models agree with observations? Philosophical Transactions of the Royal Society A., 373, 20140164, doi:10.1098/rsta.2014.0164.

Opfergelt, S., Burton, K. W., Pogge von Strandmann, P. A. E., Gislason, S. R., and Halliday, A. N., (2013). Riverine silicon isotope variations in glaciated basaltic terrains: Implications for the Si delivery to the ocean over glacial-interglacial intervals. Earth and Planetary Science Letters, 369–370, 211–219, doi:10.1016/j.epsl.2013.03.025.

Peltier, W. R. (1994). Ice age paleotopography. Science, 265(5169), 195-201, doi:10.1126/science.265.5169.195.

Pichevin. L. E., Reynolds, B. C., Ganeshram. R. S., Cacho, I., Pena, L., Keefe, K., and Ellam, R. M., (2009). Enhanced carbon pump inferred from relax-

©2020 American Geophysical Union. All rights reserved.

ation of nutrient limitation in the glacial ocean. Nature, 459, 1114–1117, doi:10.1038/nature08101.

Pondaven, P., Ruiz-Pino, D., Fravalo, C., Tréguer, P., and Jeandel, C., (2000). Interannual variability of *Si* and *N* cycles at the time-series station KERFIX between 1990 and 1995 - a 1-D modelling study. Deep Sea Research I, 47, 223–257, doi:10.1016/S0967-0637(99)00053-9.

Ragueneau, O., Tréguer, P., Leynaert, A., Anderson, R. F., Brzezinski, M. A., DeMaster, D. J., Dugdale, R. C., Dymond, J., Fischer, G., François, R., Heinze, C., Maier-Reimer, E., Martin-Jézéquel, V., Nelson, D. M., and Quéguiner, B., (2000). A review of the Si cycle in the modern ocean: recent progress and missing gaps in the application of biogenic opal as a paleoproductivity proxy. Global and Planetary Change, 26, 4, 317–365, doi:10.1016/S0921-8181(00)00052-7.

Rahman, S., Aller, R. C., and Cochran, J. K., (2017). The Missing Silica Sink: Revisiting the Marine Sedimentary Si Cycle Using Cosmogenic ^{32}Si. Global Biogeochemical Cycles, 31, 1559–1578, doi:10.1002/2017GB005746.

Reynolds, B. C., (2009). Modeling the modern marine δ^{30}Si distribution. Global Biogeochemical Cycles, 23, GB2015, doi:10.1029/2008GB003266.

Reynolds, B. C., Frank, M., and Halliday, A. N., (2006). Silicon isotope fractionation during nutrient utilization in the North Pacific. Earth and Planetary Science Letters, 244, 431–443, doi:10.1016/j.epsl.2006.02.002.

Richter, F. M., and Turekian, K. K., (1993). Simple models for the geochemical response of the ocean to climatic and tectonic forcing. Earth and Planetary Science Letters, 119, 1-2, 121–131, doi:10.1016/0012-821X(93)90010-7.

Rosenthal, Y., Boyle, E. A., and Labeyrie, L., (1997). Last glacial maximum paleochemistry and deepwater circulation in the Southern Ocean: Evidence from foraminiferal cadmium. Paleoceanography, 12, 6, 787–796, doi:10.1029/97PA02508.

Schoelynck, J., Subalusky. A. L., Struyf, E., Dutton, C. L., Unzué-Belmonte, D., Van de Vijver, B., Post, D. M., Rosi, E. J., Meire, P., and Frings, P., (2019). Hippos (*Hippopotamus amphibius*): The animal silicon pump. Science Advances, 5, 5 1–10, doi:10.1126/sciadv.aav0395 .

Sime, L. C., Kohfeld, K. E., Le Quéré, Wolff, E. W., de Boer, A. M., Graham, R. M., and Bopp, L., (2013). Southern Hemisphere westerly wind changes during the Last Glacial Maximum: model-data comparison. Quaternary Science Reviews, 64, 104–120, doi:10.1016/j.quascirev.2012.12.008.

Stoll, H., (2020). 30 years of the iron hypothesis of ice ages. Nature, 578, 370–371, doi:10.1038/d41586-020-00393-x.

Sutton, J. N., Varela, D. E., Brzezinski, M. A., and Beucher, C. P., (2013). Species-dependnt silicon isotope fractionation by marine diatoms. Geochimica et Cosmochimica Acta, 104, 300-309, doi:10.1016/j.gca.2012.10.057.

Sutton, J. N., André, L., Cardinal, D., Conley, D. J., de Souza, G. F., Dean, J., Dodd, J., Ehlert, C., Ellwood, M. J., Frings, P. J., Grasse, P., Hendry, K., Leng, M. J., Michalopoulos, P., Panizzo, V. N., and Swann, G. E. A., (2018). A Review of the Stable Isotope Bio-geochemistry of the Global Silicon Cycle and Its Associated Trace Elements, Frontiers in Earth Science, 5, 112, doi:10.3389/feart.2017.00112.

Tréguer, P., Nelson, D. N., Van Bennekom, A. J., DeMaster, D. J., Leynaert, A., and Quéguiner, B., (1995). The Silica Balance in the World Ocean: A Reestimate. Science, 268, 5209, 375–379, doi:10.1126/science.268.5209.375 .

Tréguer, P. J., and De La Rocha, C. L., (2013). The World Ocean Silica Cycle. Annual Review of Marine Science, 5, 477–501, doi:10.1146/annurev-marine-121211-172346.

Weaver, A. J., Eby, M., Wiebe, E. C., Bitz, C. M., Duffy, P. B., Ewen, T. L., Fanning, A. F., Holland, M. M., Macfadyen, A., Matthews, H. D., Meissner, K. J.,

©2020 American Geophysical Union. All rights reserved.

Saenko, O., Schmittner, A., Wang, H., and Yoshimori, M., (2001). The UVic Earth System Climate Model: Model description, climatology, and applications to past, present and future climates. Atmosphere-Ocean, 39, 361–428, doi:10.1080/07055900.2001.9649686.

Wischmeyer, A. G., De La Rocha, C., Maier-Reimer, E., and Wolf-Gladrow, D. A., (2003). Control mechanisms for the oceanic distribution of silicon isotopes. Global Biogeochemical Cycles, 17, 3, 1083, doi:10.1029/2002GB002022.

Accepted Article

©2020 American Geophysical Union. All rights reserved.